Improved microparticle electrodynamic ion traps for physics teaching

Kenneth G. Libbrecht, and Eric D. Black

Citation: American Journal of Physics **86**, 539 (2018); doi: 10.1119/1.5034344
View online: https://doi.org/10.1119/1.5034344
View Table of Contents: http://aapt.scitation.org/toc/ajp/86/7
Published by the American Association of Physics Teachers

APPARATUS AND DEMONSTRATION NOTES

The downloaded PDF for any Note in this section contains all the Notes in this section.

John Essick, *Editor*
Department of Physics, Reed College, Portland, OR 97202

This department welcomes brief communications reporting new demonstrations, laboratory equipment, techniques, or materials of interest to teachers of physics. Notes on new applications of older apparatus, measurements supplementing data supplied by manufacturers, information which, while not new, is not generally known, procurement information, and news about apparatus under development may be suitable for publication in this section. Neither the *American Journal of Physics* nor the Editors assume responsibility for the correctness of the information presented.

Manuscripts should be submitted using the web-based system that can be accessed via the *American Journal of Physics* home page, http://ajp.dickinson.edu and will be forwarded to the ADN editor for consideration.

Improved microparticle electrodynamic ion traps for physics teaching

Kenneth G. Libbrecht[a] and Eric D. Black[b]
264-33 Caltech, Pasadena, California 91125

(Received 17 December 2017; accepted 1 April 2018)

We review the essential physics of microparticle electrodynamic ion traps (MEITs) and suggest several improvements in the design, construction, and application of MEITs in undergraduate physics teaching. Pulling together insights gleaned from a number of disparate sources, we have developed MEITs with better overall performance and reliability in comparison to previous publications. This work builds upon a long history of MEIT advancement over many decades, further lowering the barriers to using these fascinating devices in physics teaching labs and demonstrations.
https://doi.org/10.1119/1.5034344

I. INTRODUCTION

Electrodynamic ion traps (EITs), also known as Paul traps or quadrupole ion traps, guide the motion of charged particles using time-varying electric fields, thus confining charged particles in free space. Wolfgang Paul and Hans Dehmelt received the Nobel Prize for Physics in 1989 for developing ion trapping, and the technology is in widespread use today. Applications of atomic and molecular ion traps in physics and chemistry include precision mass spectrometry,[1] quantum computing,[2] and improved atomic frequency standards.[3] In these applications, EITs typically operate using radiofrequency electric fields in vacuum, and they have been well studied over many decades.[1,4,5] Microparticle electrodynamic ion traps (MEITs) are also commonly used to measure the detailed properties of individual charged particles in the 100-nm to 100-μm size range, including aerosols,[6,7] liquid droplets,[8,9] solid particles,[10,12,13] nanoparticles,[14,15] and even microorganisms.[16,17]

MEITs are an excellent addition to physics teaching labs and lecture demonstrations as well, as they provide a fascinating demonstration of oscillatory mechanics and electric forces–both fundamental topics that are taught quite early in undergraduate curricula. Moreover, MEITs are inexpensive to construct, easy to use, and captivating to watch, making them well suited for a teaching environment.[10,11,18,19] Beyond individual particles, MEITs can also trap large numbers of charged particles that self-organize into Coulomb crystalline structures.[10,19,20]

We recently developed a series of MEIT experiments for use in undergraduate teaching labs,[21] trapping 26-μm-diameter particles in air using 60 Hz electric fields with electrode voltages up to 6 kV. Load resistors limit all currents to below one mA, making the high-voltage hardware safe for student use. The MEITs themselves are a few centimeters in size, and the particles are illuminated using laser light to make them easily visible to the naked eye.

During our development process, we accumulated a number of valuable insights relating to MEIT design, construction, and operation. Some of these insights are only hinted at in the scientific literature, and others appear only in online videos and other impermanent and hard-to-locate sources (described in detail below). Taken together, these insights greatly improved the performance, reliability, and safety of our MEIT experiments. We now easily trap large numbers of particles in "Coulomb clouds" using a simple ring electrode geometry, and several examples are shown in Fig. 1. A principal goal of this paper is to document our experimental methods in detail, as we believe there is much room for additional improvements and creative implementation of MEITs in undergraduate teaching.

II. BASIC ION TRAPPING THEORY

We begin with an introduction to the physics of electrodynamic ion traps, focusing on trapping microparticles in air using 60-Hz electric fields. Many ion-trapping research papers jump quickly to the Mathieu equation to describe the particle dynamics, but that approach (in our opinion) needlessly obscures the underlying physical concepts. Ion trapping requires little more theoretical background than basic mechanics with Coulomb forces, and thus is quite accessible to beginning physics students and non-physics majors. As

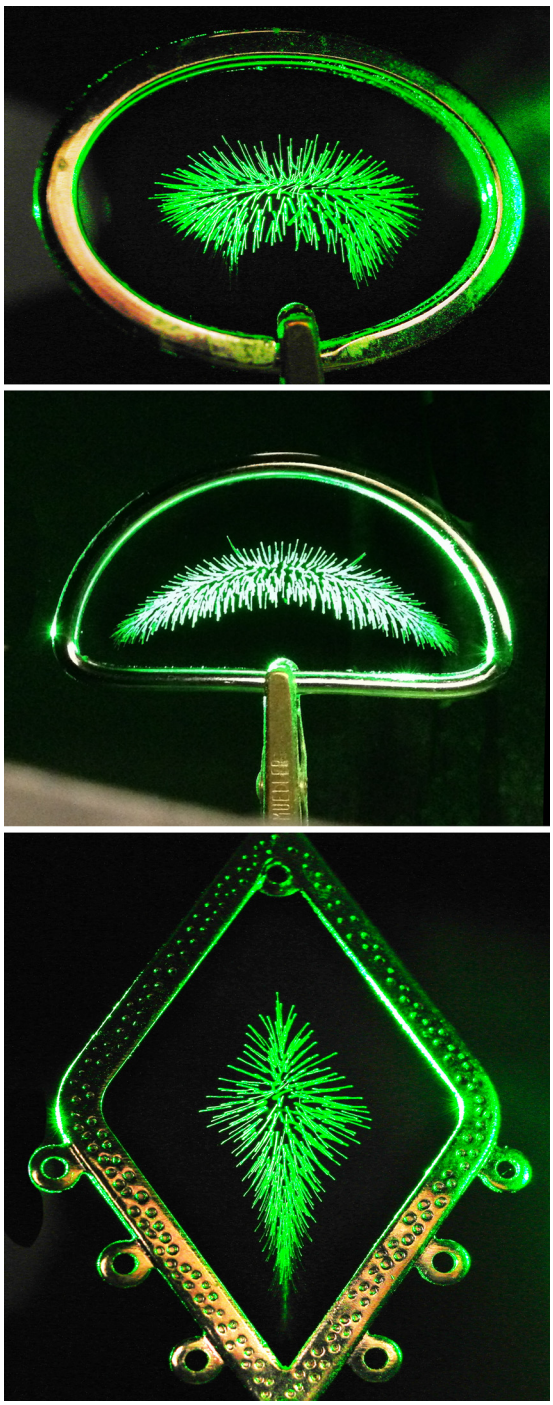

Fig. 1. These three photographs show collections of 26-μm-diameter particles trapped in air by ring-type microparticle electrodynamic ion traps (MEITs). Each trap consists of a planar conducting ring electrode held by an alligator clip delivering a voltage of 6 kV AC at 60 Hz. The particles are negatively charged Lycopodium club-moss spores illuminated with laser light. The electric field geometry and trapping forces are described in detail in the text. The particles exhibit oscillatory motions that make them appear as streaks of light in these photos. The inward trapping forces are countered by the mutual Coulomb repulsion between the particles, resulting in an expanded "Coulomb cloud" with an overall shape defined by the different ring geometries. The oval key ring (top), D buckle (middle), and diamond-shaped earring (bottom) have maximum horizontal inner diameters of 30, 38, and 22 mm, respectively.

we show below, electrodynamic ion trapping can even be described qualitatively using minimal mathematics along with some physical intuition. Because charged-particle trapping using oscillatory forces is a nontrivial result, electrodynamic ion trapping gives students an intriguing look at what is possible when $F = qE$ is taken beyond simple static situations.

A. Earnshaw's theorem

The basic idea of an ion trap is to confine a charged particle in free space (away from any other matter) using electric fields alone. Samuel Earnshaw showed in 1842 that stable trapping was not possible using static fields, a result now known as *Earnshaw's theorem*.[22] The essential proof is relatively simple (given the benefit of post-1842 physics). To trap a positively charged particle at some position in space using only static electric fields, all the electric field vectors around that position would have to be pointing inward. Gauss's Law tells us that this is impossible unless there is a net negative charge at that position. Thus a static electric field geometry cannot stably trap a charged particle in free space.

There are magnetic variations of Earnshaw's theorem as well, stating that a bar magnet cannot be trapped in free space using only static magnetic fields.[23,24] Adding gravity does not improve matters, and another extension of Earnshaw's theorem states that neither charged particles nor magnets can be stably levitated against gravity using static fields alone.

Fortunately, there are many routes around Earnshaw's theorem. One popular engineering method is to use active feedback. In the magnetic case, for example, one can continually measure the position of a levitated magnet and adjust the forces appropriately to keep the magnet stably positioned in free space, which is done in applications ranging from magnetically levitated trains to magnetically levitated toys. Another way around Earnshaw's theorem for magnetic levitation is to use a spinning magnet (possessing non-zero angular momentum) instead of a stationary one. A toy called the *Levitron* demonstrates levitation of a spinning magnet without using active feedback, and magnetic atom traps work using similar principles.[23]

Paul and Dehmelt got around Earnshaw's theorem by using oscillating electric fields to trap charged particles, as the theorem strictly applies only to static fields. Levitating bar magnets using oscillating magnetic fields has also been demonstrated.[24] It is not immediately obvious that you can use oscillating fields to trap particles (hence the Nobel Prize), so our first task as educators is to describe the basic physics underlying electrostatic ion trapping as simply as possible.

B. A mathematics-free (almost) description

1. Particle motion in a uniform, oscillating electric field

To begin, consider a charged particle placed inside an ideal parallel-plate capacitor, as shown schematically in Fig. 2. Assume that the plates are large compared to their separation, and there is a vacuum between the plates. Assume also that a sinusoidally oscillating voltage is applied across the plates, giving a uniform oscillating electric field $E(t)$ between the plates, as shown in the figure. The particle with charge q is placed between the plates at some position z, with zero initial velocity. The electric force on the particle is given by $F = qE$, and we will ignore the gravitational force. Because the electric field oscillates and thus reverses

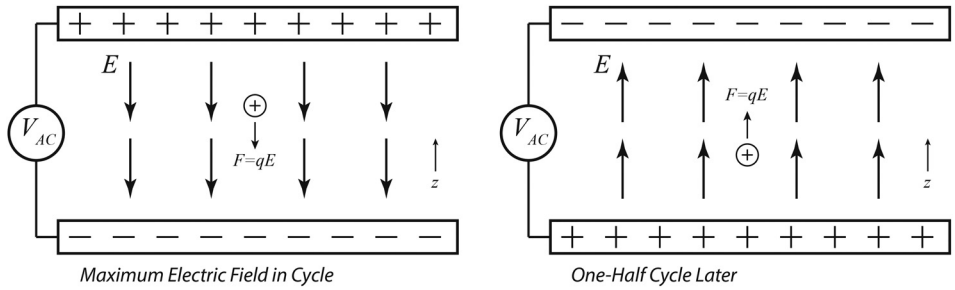

Fig. 2. These diagrams show a charged particle placed initially at rest inside a parallel-plate capacitor. An oscillating voltage is applied to the capacitor, so the electric field oscillates with time, but is always uniform between the plates. The field causes the particle position to oscillate, and two times are shown in these two sketches. Note that when the particle position z is high (left), the electric field pushes it down. When the particle z is low (right), the electric field pushes it back up. The average particle position $\langle z \rangle$ remains constant.

direction with time, so does the force on the particle, and the particle is pushed up and down as the force on it oscillates. And because the electric field is spatially uniform between the plates, the net force averages to zero over a single cycle. The particle thus oscillates up and down with some fixed average position $\langle z \rangle$.

It is customary to divide the particle motion into two parts: (1) the *micromotion* that occurs on 60-Hz time scales, and (2) the *secular motion* that is averaged over several oscillation periods. In Fig. 2, the oscillating electric field causes a micromotion, but no long-term secular motion, because it is spatially uniform.

2. Adding an electric field gradient

Now we make the problem a bit richer by adding a small electric field gradient, so the field is no longer uniform in space. One way to add a field gradient is by curving the plates of our capacitor a small amount, as shown in Fig. 3. For example, the two plates in the figure might be sections of spherical shells, where the geometrical centers are both located at the same point high above the plates. The details of the plate geometry are not especially important. What is important is that the electric field lines look roughly like those shown in Fig. 3–in particular, the field strength near the top plate is higher than near the bottom plate (as shown by the lengths of the field vectors in the figure).

Because the plates are only curved a small amount, the electric fields differ only slightly from the parallel-plate example shown in Fig. 2. The particle motion, therefore, is about the same as it was before, so the particle mainly oscillates about its initial position. But now we can see, from the geometry in Fig. 3, that the force on the particle over one cycle no longer averages to zero (although the force at any stationary point does average to zero, the particle is not stationary). As shown in the figure, when z is above $\langle z \rangle$ (left side of the figure), the particle experiences a stronger-than-average electric field pushing it downward. And when z is below $\langle z \rangle$ (right side of the figure), the upward force is weaker than average. This imbalance was not present in Fig. 2. From this fairly basic reasoning, shown graphically in Fig. 3, we can deduce that there is a net, time-averaged *secular* force pushing the particle down, often called a *ponderomotive force*. Put another way, the force averaged over many oscillation cycles pushes the particle toward a region where the oscillating electric field is weaker.

3. Quadrupole ion traps

With this basic understanding of how particles behave in oscillating electric fields, we can proceed to make an ion trap by considering more complex field geometries. We will focus on what are called *quadrupole ion traps*, looking at both 3D and 2D varieties. One easy way to make a 3D quadrupole trap is shown in Fig. 4. An AC voltage with angular frequency Ω is applied to two ball-shaped electrodes in a grounded box, creating oscillatory electric fields inside the box. Halfway between the balls, the electric field is always zero by symmetry. Near this zero-field point, the electric fields at one point in the AC cycle are shown in the figure. Multiply these vectors by $\sin(\Omega t)$ to obtain the electric fields at other times.

With this field geometry, the electric field strength increases in all directions outward from the zero-field point halfway between the balls. Because the time-averaged electric forces push particles toward regions where the

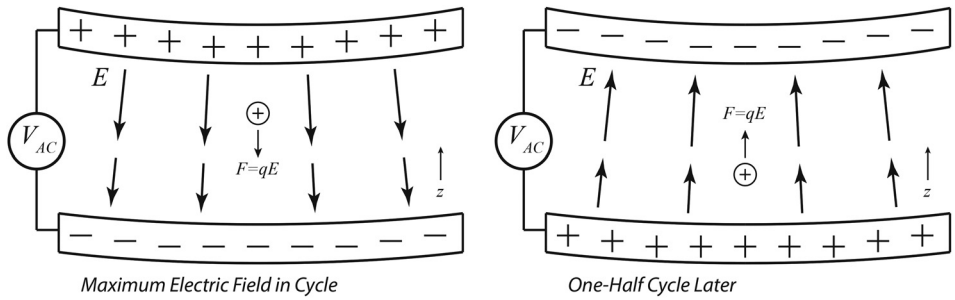

Fig. 3. A charged particle placed initially at rest inside a curved-plate capacitor. The geometry of the plates causes a gradient in the electric field strength, so that the field is stronger for larger z (as shown by the longer arrows in the diagrams) This imbalance means that the electric force on the particle is stronger at the top of its motion (left) and weaker at the bottom (right). Averaging over time, there is a net force that pushes the particle down, toward the weaker-field region.

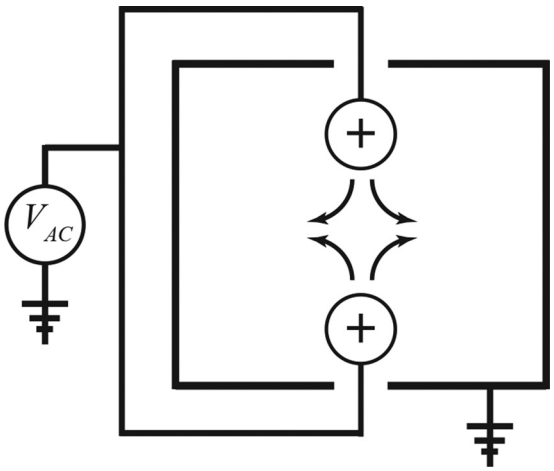

Fig. 4. This diagram shows one method for making a 3D quadrupole ion trap, using two ball-shaped electrodes in a grounded box. When the balls are at a positive potential relative to the box, as shown here, the electric field lines are given roughly by the arrows. A half-cycle later, the balls are at a negative potential relative to the box, and the field lines are reversed. By symmetry, the electric field halfway between the balls is always zero. The electric field geometry between the balls is essentially as drawn here even if the grounded walls of the box are expanded out to infinity.

oscillating electric field is weaker, particles become trapped at the center point. The qualitative force argument shown graphically in Fig. 3 strictly only applies to the $r = 0$ line and the $z = 0$ plane in the ball-trap (taking $r = z = 0$ at the center point between the balls). One can, however, draw pictures similar to those in Fig. 3 that examine a particle placed at other locations in the trap, for example, when $r = z \neq 0$. Doing this quickly reveals that the time-average of the (vector) electric force again pushes the particle toward the trap center at $r = z = 0$. Thus we see that the micromotion is zero at the trap center, increasing in all directions away from this point, while the time-averaged secular forces push particles toward the trap center.

Another approach for making a 3D quadrupole trap is the *ring trap* shown in Fig. 5. Again the electric field at the center of the ring is always zero, and the arrows show the fields in the vicinity of this central region at one point in the cycle. Both these examples show electric field geometries that: (1) have zero electric field at a center point, (2) have field magnitudes that increase in all directions away from the central point, and (3) exhibit axial symmetry.

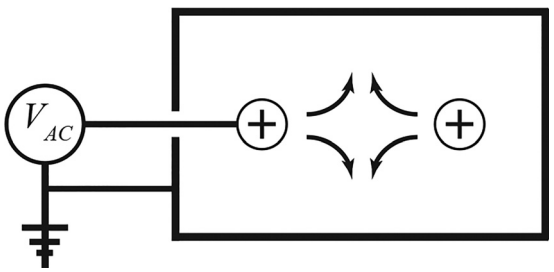

Fig. 5. This diagram shows another method for making a 3D quadrupole trap. In this configuration a ring electrode (seen edge-on here) is placed inside a grounded box, and the potential between the two is set by an applied AC voltage. As in Fig. 4, the electric field at the ring center is always zero by symmetry. Also, the electric field geometry near the ring center is essentially as drawn here even if the grounded walls of the box are expanded out to infinity.

With the above qualitative description, it is possible to explain ion trapping while standing at the chalkboard, using vector diagrams and essentially no equations. All that is required is a basic understanding of mechanics and electric forces. The most difficult concept is the quadrupole field geometry. Interestingly, our intuitive feel for electric-field geometries appears to have come entirely (or almost entirely) from seeing vector field diagrams in physics classes, in physics demonstrations, and in textbooks. The actual calculation of these vector plots is nontrivial and is learned much later in physics curricula. A discussion of electrodynamic ion trapping, therefore, helps to establish and reinforce this learned intuition.

C. A basic mathematical description

To quantify the above qualitative description, assume that the plates in Fig. 2 are separated by a distance d, and the applied voltage is $V(t)$. As long as the fields do not change too rapidly, we can assume a uniform electric field in the space between the plates equal to $E(t) = V(t)/d$. Assume a sinusoidally oscillating voltage, $V(t) = V_0 \sin \Omega t$, which gives an electric field between the plates $E(t) = E_0 \sin \Omega t$, with $E_0 = V_0/d$. The time-dependent electric force on the particle is $F(t) = qE(t) = qE_0 \sin \Omega t$, and solving this equation of motion gives the particle position

$$z(t) = z_{init} + v_{init}t - \frac{qE_0}{m\Omega^2} \sin \Omega t, \tag{1}$$

where z_{init} is the initial position of the particle and v_{init} is its initial velocity.

Adding a field gradient and taking $z_{init} = v_{init} = 0$, the force on the particle becomes

$$F(z,t) = q(E_0 + E'z) \sin \Omega t, \tag{2}$$

where $E' = dE/dz$. For small E', we substitute the micromotion in Eq. (1) as an approximation for $z(t)$ in Eq. (2), giving the approximate time-averaged (secular) force

$$\langle F \rangle \approx -\frac{q^2 E' E_0}{2m\Omega^2} \tag{3}$$

which is accurate to lowest order in E'. The negative sign in this expression means that $\langle F \rangle$ pushes the particle toward a region of weaker electric field. Note also that the trapping force is independent of the sign of the charge.

A convenient way to describe this situation uses a *trap pseudopotential*, which is simply the kinetic energy of the micromotion: $U_{trap} = (KE)_{micromotion} = \frac{1}{2} m \langle v^2_{micromotion} \rangle$. Using $\langle v^2_{micromotion} \rangle = q^2 E^2 / 2m^2 \Omega^2$ from Eq. (1), we obtain that the secular force in the vertical direction, $\langle F \rangle = dU_{trap}/dz$, reproduces Eq. (3) in the example above. It turns out that $\langle F \rangle$ is equal to the gradient of the pseudopotential in all three dimensions (for example, in a quadrupole electric field geometry), but proving this is beyond the scope of this paper. A general derivation of the pseudopotential $U_{trap} = (KE)_{micromotion}$, along with a careful consideration of the underlying assumptions, is given in Ref. 25 (Section 30).

D. Quadrupole field geometries

We can quantify the quadrupole electric field geometries by looking at the field near the trap center. A multipole

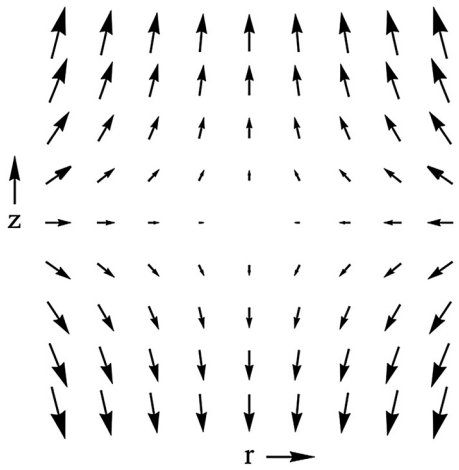

Fig. 6. A vector plot of the 3D quadrupolar electric field geometry, showing the electric field vectors when the applied voltage is at its maximum. Multiply each vector by $\cos(\Omega t)$ to obtain the electric fields at other times. Note that the field amplitude in the z direction (along $r=0$) is double that in the r direction (for $z=0$). Both the ring trap and the single-particle trap described in the text have this field geometry near the trap center.

expansion of a 3D quadrupole trap gives an electric potential near $r=z=0$

$$V(r,z)_{3D-Quad} = A_0 + A_2[2z^2 - r^2]\cos\Omega t,$$

where A_0 and A_2 are constants, with the electric field components

$$\begin{aligned} E_z &= -\frac{\partial V}{\partial z} = -4A_2 z\cos\Omega t \\ E_r &= -\frac{\partial V}{\partial r} = 2A_2 r\cos\Omega t \end{aligned} \tag{4}$$

and a vector plot is shown in Fig. 6. Note that the electric field strength increases linearly with r and z as one goes out from the origin.

For a 2D quadrupole trap, we have

$$V(x,y)_{2D-Quad} = A_0 + A_2\left[x^2 - y^2\right]\cos\Omega t$$

giving the electric field components

$$\begin{aligned} E_x &= -\frac{\partial V}{\partial x} = -2A_2 x\cos\Omega t \\ E_y &= -\frac{\partial V}{\partial y} = 2A_2 y\cos\Omega t. \end{aligned} \tag{5}$$

Rotating the potential by 45° in the xy plane gives a similar-looking expression

$$\begin{aligned} E_x &= -2A_2 y\cos\Omega t \\ E_y &= -2A_2 x\cos\Omega t \end{aligned} \tag{6}$$

and a vector plot is shown in Fig. 7. Again we see that the electric field strength increases linearly with x and y near the origin.

E. Damped ion traps

Damping is important for our MEITs operating in air, so we add a viscous damping force $F=-\gamma v$, where γ is the usual damping constant and v is the particle velocity. The one-dimensional case can be computed in much the same way as we described above, giving the secular force

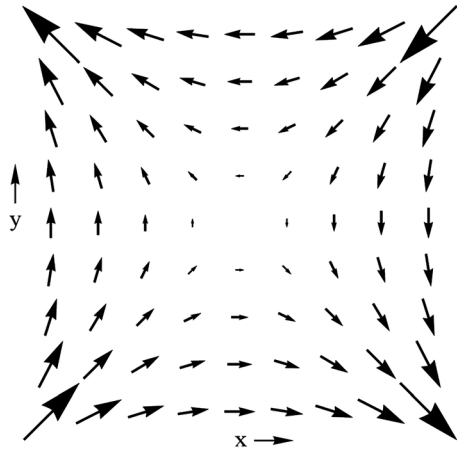

Fig. 7. The 2D quadrupolar electric field geometry, again plotting the electric field vectors at one point in time. The "4-bar" linear trap described in the text has this field geometry near its central axis.

$$\langle F\rangle \approx -\frac{q^2 E' E_0}{2m}\frac{1}{\Omega^2+\Gamma^2}, \tag{7}$$

where $\Gamma=\gamma/m$, and this reduces to Eq. (3) in the absence of damping. The same result can also be obtained using the pseudopotential U_{trap} described above.

1. Stokes damping

To calculate the damping constant, we first note that the Reynolds number of the particle motion is quite small, given by $R_e \approx \rho_{air} v R/\mu_{air} \approx 0.05$, where $\rho_{air} \approx 1.2\,\text{kg/m}^3$ is the air density, $v \approx 1\,\text{mm}/(1/60\,\text{s}) \approx 6\,\text{cm/s}$ is a typical observed particle micromotion velocity in a trap, $R \approx 13\,\mu\text{m}$ is the particle radius (described below), and $\mu_{air} \approx 1.8\times10^{-5}\,\text{kg/m}\cdot\text{s}$ is the dynamical viscosity of air. For such a low Reynolds number, the air damping is well approximated by Stokes damping, given by $\gamma = 6\pi\mu R$. Assuming a particle density of $\rho_{part} \approx 500\,\text{kg/m}^3$, this gives

$$\Gamma = \frac{\gamma}{m} = \frac{9}{2}\frac{\mu}{R^2\rho_{part}} \approx 960\,\text{s}^{-1},$$

which is substantially larger than $\Omega = 2\pi(60\,\text{Hz}) = 377\,\text{s}^{-1}$. Thus the particle motion is overdamped and $\Omega^2+\Gamma^2$ in Eq. (7) can be replaced with Γ^2 to an accuracy of about 15%.

2. Trap stability

The above calculations of secular forces are useful for estimating trap forces and showing the basic trap physics. In many applications of ion trapping (e.g., molecular mass spectroscopy), another important consideration is the stability of trapped ions. In the zero damping case, stably trapped particles in an ion trap will execute complex bound orbital motions that depend on initial conditions.[5,26] As the applied trapping voltage is turned up, eventually the oscillating electric fields eject particles from the trap, so that stable trapping is no longer possible. Analyzing ion trap dynamics to

determine stability is where the Mathieu equation formalism becomes necessary.

When linear damping is added, such as Stokes damping, a trapped ion will either come to rest at the trap center (ignoring gravity or other static forces), or be ejected from the trap, as determined by an extended Mathieu-equation analysis.[27,28] Interestingly, the MEITs described below include a rich behavior of what we call "extended orbits," which require the addition of a weak nonlinear damping term in addition to Stokes damping.[28]

Obtaining a full understanding of ion trap dynamics, including nonlinear dynamics, is still an area of active research, and it lies beyond what is typically presented in undergraduate curricula. However, the basic trap analysis described above shows that the essential EIT physics is mainly mechanics and electric forces, topics that are taught in early college physics courses. For this reason, ion traps provide a useful tool for connecting basic physics concepts to a nontrivial and quite fascinating application. A mention of trap stability, mass spectroscopy, and nonlinear dynamics has pedagogical merits as well, in that it informs students that physics remains a dynamic subject where relatively simple concepts factor into many modern applications. Our attention now turns to methods and practices that are useful when constructing MEITs for applications in physics teaching.

III. MEIT DESIGN AND CONSTRUCTION

As mentioned in the introduction, the use of MEITs in physics education has been presented in the literature numerous times.[10,18–20] With these papers as a starting point, we begin by describing several insights we have gained during the design and construction of our own ion trapping experiments.

A. Laser illumination

Individual particles in the 10–30 μm size range are very difficult to see with the naked eye when illuminated by ambient room lights, and trapped particles can be overlooked even with bright, directed incandescent or LED lighting. Laser illumination, however, changes this dramatically, making the particles easily visible.[29,30] We typically use inexpensive 10 mW green laser modules (which often put out 20 mW or more of 532 nm light), and we expand the beam to roughly a 1-cm size. A 1-cm beam is sufficient to illuminate all the particles in a typical ion trap, and the eye-safety concerns from such an expanded beam are no worse than with a typical green laser pointer. Laser illumination was not mentioned in many previous discussions of MEITs, and it makes a huge difference when observing trapped particles.

B. The 6 kV solution

In general, we have found that higher applied AC voltages yield more robust MEITs that are easier to use and can hold a larger numbers of particles. The improvement appears to come from trap loading considerations, although we have not explored all regions of parameter space in trap design. We believe that higher voltages mean that larger trap electrodes can be used, with an accompanying increase in the effective capture volume during loading. In our experience, trapping with 1 kV is possible but nontrivial using typical trap designs and particle charging (see below), and clear improvements are seen as the voltage is increased. Around 10 kV, however, the trap electrodes can readily arc without careful electrode design.

We have found that 6 kV of applied AC voltage is a reasonable compromise, yielding excellent trap performance with minimal arcing. Suitable commercial transformers that can produce such high voltages are both expensive and difficult to find, however, so we had our 6 kV transformers built to order, stepping 120 V up to 6 kV at 60 Hz. Very little current (typically < 0.1 mA) is needed to drive the MEITs described here, as they are basically open circuits, requiring only enough current to drive the small stray capacitance of the electrodes. A modern neon-sign "transformer" will likely not work, as these are usually switching power supplies that run at frequencies far higher than 60 Hz. Measuring the AC voltage is best done using a simple resistor divider, although care must be taken that the meter used does not load the circuit.

C. Current limiting

Although MEITs operate at high voltage, they require very little current. Thus MEITs present little electrical safety hazard *as long as sufficient current-limiting is provided*. We typically use load resistors to keep currents to below 1 mA in our MEIT designs, as this is near the limit of human detectability. Moreover, our electrodes have quite low capacitance, so the stored electrical energy is less than can be experienced from static shocks in carpeted rooms.

Figure 8 shows a relatively simple "one-electrode" trap circuit and electrode geometry, which was used to create the ion trap photos shown in Fig. 1. A pair of 10 MΩ, 10 W resistors limit the current at the output of the step-up transformer to less than 1 mA. The two resistors provide

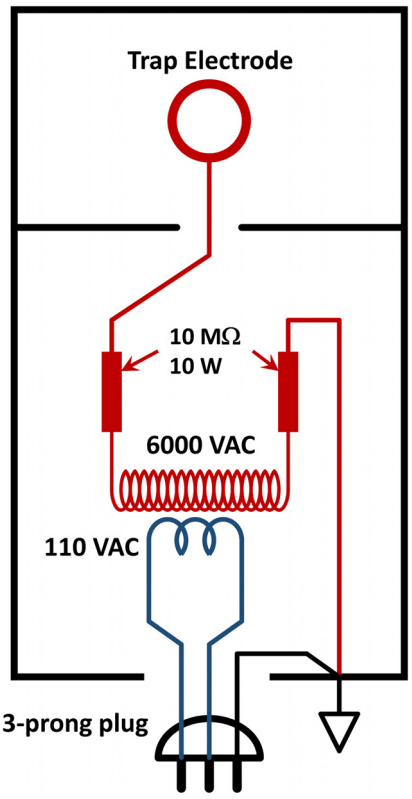

Fig. 8. This diagram shows a schematic of a basic single-electrode ion trap, with redundant current-limiting, as described in the text.

redundant safety; if one resistor shorts, the other still limits the output current. Additional safety is provided by carefully mounting the transformer and current-limiting resistors in a rugged, sealed metal enclosure that is grounded to the third prong of the AC plug. Thus if any circuit element shorts to the case, the resulting current is shunted to ground. Quite a lot would have to fail in this circuit before the trap user experienced a dangerous electrical shock. Even touching the trap electrode directly would only give a mild shock.

D. Triboelectric particle charging

The triboelectric effect provides a convenient and inexpensive method to charge particles before insertion into a MEIT. We charge the tip of a Teflon "wand" by rubbing it with cloth, and then use the wand to pick up and deliver charged particles to the trap. Holding the wand tip above the trap while tapping it to release particles is most effective. Used in this way, a Teflon wand yields negatively charged particles, while a nylon wand gives positively charged particles, as expected from the triboelectric series. We have found that Teflon is more far effective than nylon as a wand material, in that it typically delivers more particles to the traps with greater ease. This triboelectric effect provides a simple method for charging nonconducting dielectric particles and is substantially more effective than the syringe method described earlier.[18]

E. Lycopodium club moss spores

Lycopodium club moss spores are nearly ideal for trapping in MEITs, as they are inexpensive, readily available, a convenient size, nearly monodisperse, nearly spherical, easily charged, and they present essentially no safety concerns. Their use in this regard is mentioned in the comments section of Ref. 32 but we have not seen any other mention in the scientific literature. We purchased our spores online, where they are often called *Dragon's Breath*, as the particles are used to "breathe fire" in magic shows and similar events.

As shown in Fig. 9, Lycopodium club moss spores have a characteristic "sphere with a corner" shape. Approximating the particles as spheres, we measured particle diameters of $26 \pm 2.5\,\mu$m using optical microscopy, and we measured a material density of $510 \pm 40\,\mathrm{kg/m^3}$ by weighing a small beaker full of particles, assuming a random-spheres packing fraction. However, we have not done an exhaustive comparison of particle properties from different batches or different vendors. There are hundreds of known species of club moss, many quite common in temperate climates, and, to our knowledge, breathing or ingesting club moss spores in small quantities presents essentially no safety concerns. In our teaching lab, we have found that airborne Lycopodium dust may cause mild sinus irritation in some individuals, similar to that from common pollen particles.

F. Reduce air currents

The trapping forces in a MEIT are sufficiently small that air currents can easily blow particles out of a trap. This can make it difficult to trap particles in open areas like teaching labs or lecture halls without mitigating this problem. We typically surround our MEITs with enclosures that have small holes for inserting and observing particles. For the best trap stability, we block these holes completely when not in use, or cover them with optical windows.

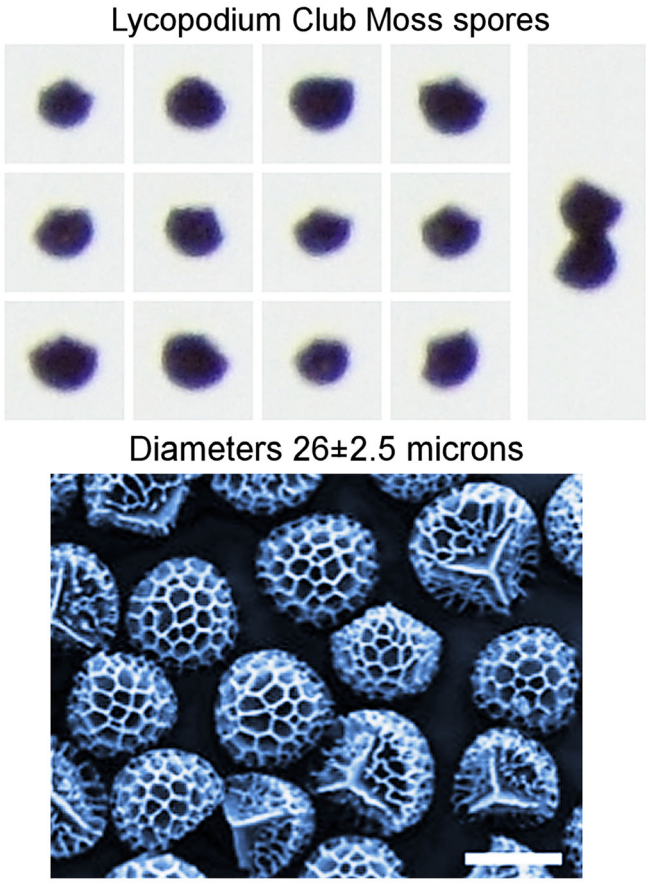

Fig. 9. The top images show a series of Lycopodium club moss spores photographed while they were trapped in a MEIT. Each of the 12 images is 57 μm square, and the particles were measured to have diameters of $26 \pm 2.5\,\mu$m. These 12 particles were trapped consecutively and were not otherwise selected. The additional image on the right shows two spores stuck together while trapped, as is occasionally seen. The lower image is a high-resolution electron micrograph of Lycopodium spores (Ref. 31), with a scale bar of 25 μm. Note that the characteristic "sphere with a corner" shape can be seen in the optical images, which have a resolution of about three microns. We measured the average material density in the spores to be $\rho = 510 \pm 40\,\mathrm{kg/m^3}$.

G. Avoid triboelectric materials in MEIT construction

Surface charging can produce sizeable spurious electric fields if plastics or other triboelectric materials are placed near the trapping region. We typically use metal construction where possible, and keep plastics away from the trapping region as much as possible. Wood and cardboard are useful materials for shielding air currents, as these materials do not develop surface charges as readily as most plastics.

H. Strobe the illumination laser

Trapped particles in a MEIT typically display a substantial micromotion, making the particles appear as short streaks of light, and these are often misinterpreted by novice observers. Strobing the illumination laser near the trapping frequency demonstrates the micromotion and is quite useful as a pedagogical tool when students first see an ion trap. Video examples can be seen elsewhere.[21]

I. Use static fields to balance gravity

Gravitational forces are sufficient to pull trapped particles substantially away from the trap center, and this effect is readily seen when a single particle is trapped. Gravity is easily balanced, however, by adding a static electric field with $qE = mg$. Modular DC-DC converters are especially useful for providing the necessary high voltages, as essentially no current is needed. We are partial to the ENCO Model GP15 module, which produces a DC output voltage $V_{out} \approx 150 V_{in}$ up to $V_{out} = 1500$ V. This unit will supply up to 0.6 mA of output current, which is more than adequate for supplying a static electric field. We typically provide additional resistive current-limiting for safety, as described above for the AC voltage.

J. The single-electrode trap

It is often beneficial to use a single trap electrode in a MEIT, letting the effective ground far from the trap serve as the second electrode. Examples are the ring traps shown in Figs. 1 and 8, or the linear "paper-clip" trap shown in Ref. 32. These trap geometries are especially open, allowing clearer views of the trapped particles than traditional trap geometries with multiple electrodes.[18] Moreover, one can be remarkably cavalier with the second electrode; it is not necessary to have a conducting grounded surface near the trapping region.

IV. THE RING TRAP

The construction insights described in Sec. III are all demonstrated in the *ring trap* shown schematically in Fig. 10. The AC electrical circuit is that from Fig. 8, which provides ample current-limit protection. A single copper ring with an inner diameter of 16 mm serves as the main trap electrode, and the ring can be rotated about a horizontal axis (by twirling the insulated handles outside the box) to provide different views the trapped particle cloud. The lower DC electrode shown in Fig. 10 provides a static electric field to roughly balance gravity. The ring electrode is surrounded by a metal enclosure that serves as an electrical ground, safety shield, and it greatly reduces air currents. An illumination laser shines down through the ring from above (not shown in Fig. 10). A cut-out in the front of the box is used to see the trap directly with the naked eye and to insert the wand for loading, and this hole is typically blocked once particles are loaded (to further reduce air currents). Trap imaging is done through a window in the back of the box.

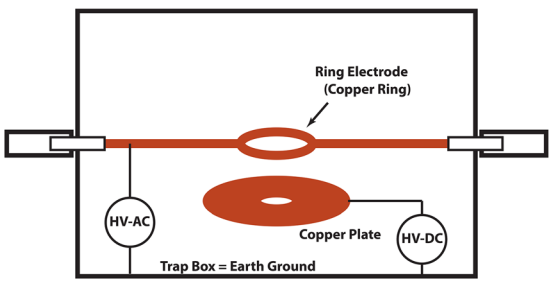

Fig. 10. This diagram shows our typical *ring trap* geometry. The main trap electrode is a copper ring (16 mm inner diameter) that can be rotated about a horizontal axis, and this is surrounded by a grounded metal enclosure. Ions are trapped near the center of the ring, as shown in Fig. 11. A conducting plate below the ring provides a static electric force to approximately balance the gravitational force.

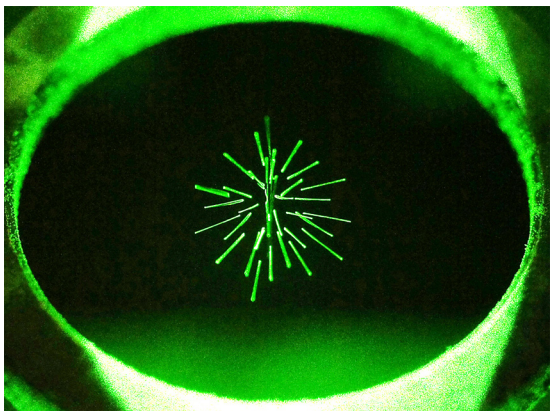

Fig. 11. This photograph shows about 30 particles held in a ring trap, which is illuminated from the top with laser light. Trapping forces push particles toward the center of the ring, while their mutual Coulomb repulsion keeps them apart. The 60-Hz micromotion makes each of the particles appear as a streak of light in this photograph, which is how they appear to the naked eye.

Figure 11 shows a small collection of particles in a ring trap, and Fig. 12 shows a much larger number of trapped particles. In our physics teaching lab, we use the ring trap as a qualitative demonstration of ion trapping physics. Students are introduced to the basic trapping theory presented above, including secular and micromotion forces, quadrupolar electric field geometries, the triboelectric effect, Coulomb crystals, and laser strobing. Students load particles into the trap (both positively and negatively charged using nylon and Teflon wands), and view the trapped particles with the naked eye and via video imaging. The AC and DC trapping fields can be varied in amplitude to examine the trap response. The DC electric fields are used to identify positively and negatively charged particles. The DC field can also balance gravity to trap a single particle with essentially no remaining micromotion at the center of the ring. The micromotion of the particles traces out the quadrupole electric field geometry, as demonstrated in Fig. 12.

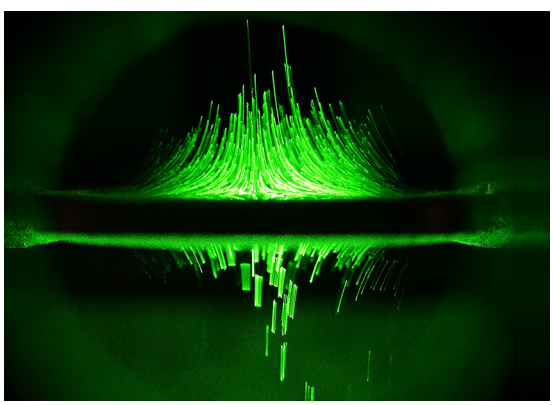

Fig. 12. This photograph shows many hundreds of particles held in a ring trap, here with the ring plane nearly horizontal. The micromotion of each particle is along the electric field, so the line segments in the photograph trace the quadrupole electric field geometry within the trap. Static electric fields can push the trapped particles above or below the ring plane.

V. THE LINEAR TRAP

Figure 13 shows a schematic layout of a *linear trap*, which traps particles along a line using a 2D quadrupolar electric field geometry. Teflon end caps develop a negative surface charge as the trap is used (presumably as negatively charged particles impinge upon the inner surface of the tubes), and this charge is sufficient to weakly trap negatively charged particles in the axial direction. Here again we exploit the triboelectric effect as an inexpensive method for providing the desired axial electric fields. For both the linear and ring traps, students can literally poke at the trapped particles with the charged wand to see how this affects the trapping.

Figure 14 shows a linear trap being used to create a one-dimensional Coulomb crystal. After loading a large number of particles in the trap (top photo), we then adjusted HV-DC (see Fig. 13) to approximately balance gravity. Lowering HV-AC then caused particles with lower-than-average q/m to fall down and out of the trap, while particles with higher-than-average q/m were pulled up and out of the trap. The remaining particles then had similar q/m, and therefore similar m because the Lycopodium particles are approximately monodisperse (as seen in Fig. 9). Increasing HV-AC then traps the particles close to the trap axis, yielding the linear array of particles seen in the lower photo in Fig. 14.

In our physics teaching lab, we use the linear trap as another qualitative demonstration of ion trapping physics. Students are introduced to the linear trapping geometry and one-dimensional Coulomb crystals. Additional nonlinear effects are also demonstrated in the linear trap, and these effects are described in detail in Ref. 28. We also discovered the "trapnado" phenomenon in our linear traps,[21,28] providing an especially dramatic example of how many-body effects can lead to nontrivial emergent phenomena, reminding students that future physicists have much to ponder even in relatively simple physical systems.

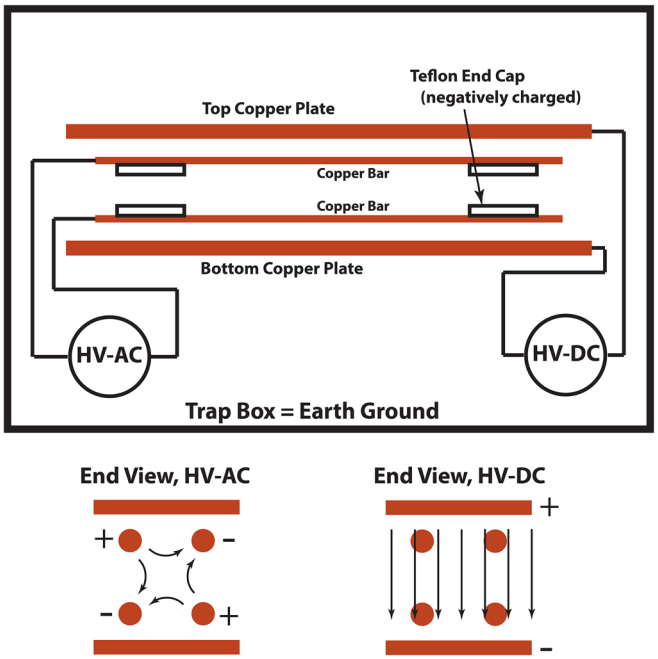

Fig. 13. These diagrams show a "4-bar" linear ion trap. The AC and DC electric fields are shown qualitatively in the lower diagrams, which show views along the horizontal trap axis. The top diagram shows a face-on view of the trap. The four trap bars have diameters of 3.2 mm, with a closest separation of 9.5 mm.

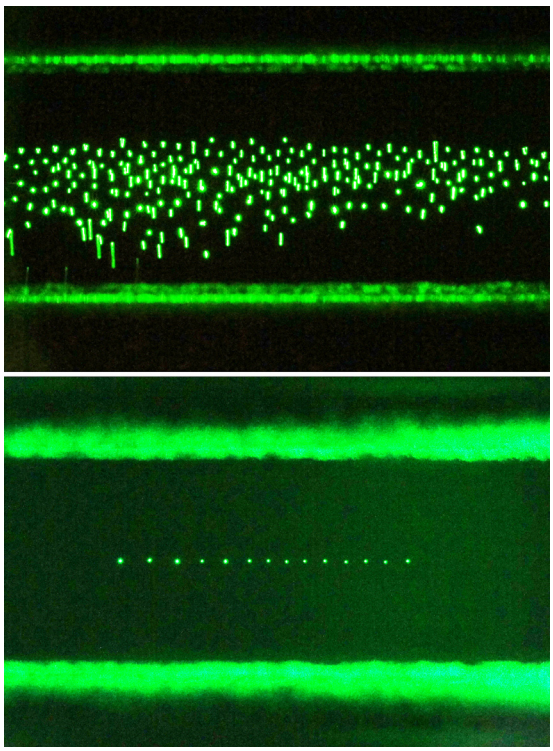

Fig. 14. The top photograph shows a large number of particles held in a linear trap, illuminated with laser light. Trapping forces push particles toward the horizontal trapping axis, while their mutual repulsion keeps them separated. The diffuse horizontal lines above and below the trapped particles are from the bar electrodes. The lower image shows 14 particles in a linear Coulomb crystal. Trapping forces keep the particles along the trap axis, and gravity is balanced by static electric forces. The particles are pushed together by weak axial electric fields, and they are held apart by mutual Coulomb repulsion.

VI. THE SINGLE-PARTICLE TRAP

To go beyond qualitative ion trapping phenomena and into quantitative measurements in the teaching lab, we use the *single-particle trap* shown schematically in Fig. 15. This trap incorporates a built-in microscope objective (not shown in the figure) that is capable of imaging trapped particles with a resolution of about three microns. Sample images from the microscope are shown in Fig. 9, using LED backlighting (which generally produces sharper images than

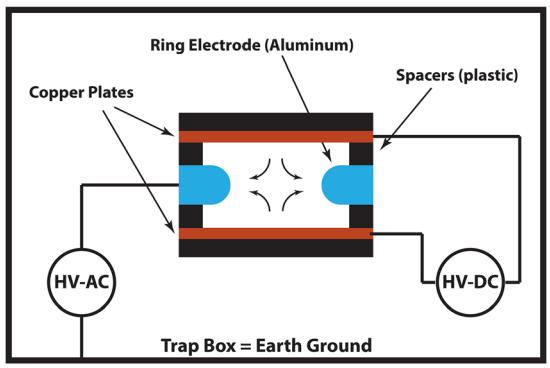

Fig. 15. A schematic diagram of the single-particle trap described in the text. The ring electrode is an aluminum plate with a 9.5-mm-diameter central hole, and this is flanked by parallel copper plates (seen edge-on in this diagram; separated by 12.7 mm). Numerical modeling of the axially symmetric electrode geometry relates the electric fields to the applied voltages.

using monochromatic laser light). In this trap geometry, the DC electric field is linearly proportional to the applied voltage HV-DC with a proportionality constant we obtained using a numerical electrostatics model of the system. The constant A_2 in Eq. (4) is similarly calculated from numerical modeling of the electrode geometry.

The micromotion of a single trapped particle is eliminated when the static electric force balances gravity, and this can be readily observed in the microscope video image. The force balance $qE = mg$ then gives the charge-to-mass ratio q/m for a known applied field E. Imaging the particle gives its radius to an accuracy of about 20%, allowing students to calculate the particle mass m from the known material density. Putting the different observations together thus yields the charge q to an overall accuracy of around a factor of two.

Typical measurements yield particle charges on the order of 10^5 times the electron charge, with a maximum value around $q_{max} \approx 3 \times 10^5$ electron charges. There seems to be no lower charge limit, although particles with charges much below $q_{max}/10$ are difficult to support in the trap against gravity. The calculated surface electric field strength on a Lycopodium particle with $q \approx q_{max}$ is roughly equal to the ionization breakdown field in air. This suggests that ionization will pull charge off a particle if $q > q_{max}$, thus providing a practical upper limit to particle charging that depends on the particle size.

VII. DISCUSSION

Having incorporated the various design insights described above, we found that our MEITs were remarkably robust and easy to use. Add to that their simplicity, relatively low cost, intriguing physics content, and overall student appeal, and we believe that ion trapping has a great deal of unrealized potential as a physics teaching tool. Moreover, we believe that ion trapping is brimming with possibilities for intriguing student-led projects with varying levels of difficulty. A few examples include:

(1) Measuring light pressure effects. The gravitational force on a Lycopodium spore is approximately 50 pN, equal to the light force from absorbing a 15 mW laser beam. Moreover, gravity is a large and easily observed force in the MEITs described above. With some care, it should be possible to detect forces down to 100 fN or lower in a specially designed MEIT. Thus one should be able to observe light pressure effects using nothing more than a common laser pointer. While this would not be an especially easy or inexpensive experiment, it may end up being cheaper, safer, and more quantitative than the optical-tweezer experiments that have become somewhat popular in physics teaching.
(2) Measuring the fundamental charge. A single electron charge in a static field of 10^6 V/m ($3\times$ below a typical breakdown field) experiences a force of $qE = 160$ fN. With additional improvements in trap design, we can imagine a MEIT-based experiment capable of measuring the fundamental charge more reliably than the venerable (but difficult) Millikan oil-drop experiment. Observing discrete charge jumps (for example, from cosmic rays) on a single MEIT particle would confirm the discrete nature of charge without having to make a precise charge measurement.
(3) Exploring different particle materials. Trapping Lycopodium club moss spores in MEITs is a substantial design advance, in our opinion, as these particles allow easier trap operation compared to other choices. However, searching for still better pollen-like particles could be a worthwhile research effort.
(4) Examining *in situ* charging and discharging. An individual particle in a MEIT is easily stable for days or weeks,[18] but it may be interesting to explore charging or discharging mechanisms, perhaps as a function of particle micromotion, UV illumination, humidity, and other factors. Cold-cathode emission from a thin, sharpened wire placed near a trapped particle may have interesting effects as well. Here again, discovering ways to control the charge on trapped particles could be highly beneficial for developing the next generation of educational MEITs.
(5) Investigations of nonlinear dynamics in MEITs. We scratched the surface of this topic in Ref. 28 (also see the references therein), but a great deal remains unexplored. Numerically integrating the equations of motion in a MEIT is straightforward using modern computational tools, allowing investigations of trap behavior that do not require complex analytical nonlinear mathematics.
(6) Investigating novel trap geometries. As seen in Fig. 1, even the basic ring trap can yield a variety of Coulomb cloud shapes. Creating "race track" or other trapping topologies may yield novel trap behaviors, especially in the presence of Coulomb forces between trapped particles. Investigating nonlinear trap behaviors in more complex geometries may also be fruitful.
(7) Dynamical measurements of particle properties. In the presence of damping, the trapping forces depend on particle radius via Eq. (7), and thus it should be possible to determine particle properties using dynamical measurements like micromotion. Nonlinear effects may be important also.[28] Once again, there remains significant potential for finding effects that are important for developing the next generation of MEITs.
(8) Mie scattering of spherical particles. An isolated, stationary, 25-micron-scale particle makes an excellent target for laser Mie scattering, which can be used as an independent method of determining the particle radius.
(9) Mega MEITs. While we stopped at 6 kV, proper electrode design would allow higher applied voltages, and thus still larger traps that confine more particles. Using larger particles with greater average charges may also be helpful in this regard. Establishing and documenting a record number of trapped particles could lead to some measure of YouTube renown, perhaps generating a bit of student enthusiasm in the process.

As a physics toy and instructional tool, we believe that MEITs provide a great deal of unrealized potential. Many interesting experimental and theoretical avenues have not yet been explored, and there appears to be much opportunity for involving eager physics students in developing the next generation of educational MEITs.

A number of Caltech undergraduate students contributed to the initial development of our ion traps, including Christopher Dewan, John Schulman, Giulio Rottaro, Nathaniel Indik, Gautam Upadhya, Scott Yantek, Prastuti Singh, Max Horton, and Kelly Swanson. This work was supported in part by the

California Institute of Technology and by generous donations from Drs. Richard Karp and Vineer Bhansali.

[a]Electronic mail: kgl@caltech.edu
[b]Electronic mail: blacke@caltech.edu

[1]R. E. March and J. F. Todd, *Quadrupole Ion Trap Mass Spectroscopy*, 2nd ed. (Wiley-Interscience, Hoboken, 2005).
[2]H. Haffner, C. F. Roos, and R. Blatt, "Quantum computing with trapped ions," Phys. Rep. **469**, 155–203 (2008).
[3]D. Leibfried, R. Blatt, C. Monroe, and D. Wineland, "Quantum dynamics of single trapped ions," Rev. Mod. Phys. **75**, 281–324 (2003).
[4]P. K. Ghosh, *Ion Traps* (Oxford U.P., Oxford, 1996).
[5]R. E. March, "An introduction to quadrupole ion trap mass spectrometry," J. Mass Spectrom. **32**, 351–369 (1997).
[6]M. Yang *et al*., "Real-time chemical analysis of aerosol particles using an ion trap mass spectrometer," Rapid Comm. Mass Spect. **10**, 347–351 (1996).
[7]D. T. Suess and K. A. Prather, "Mass spectrometry of aerosols," Chem. Rev. **99**, 3007–3036 (1999).
[8]B. Kramer, O. Hubner, H. Vortisch *et al*., "Homogeneous nucleation rates of supercooled water measured in single levitated microdroplets," J. Chem. Phys. **111**, 6521–6527 (1999).
[9]S. Arnold and L. M. Folan, "Fluorescence spectrometer for a single electrodynamically levitated microparticle," Rev. Sci. Instrum. **57**, 2250–2253 (1986).
[10]R. F. Wuerker, H. Shelton, and R. V. Langmuir, "Electrodynamic containment of charged particles," J. Appl. Phys. **30**, 342–349 (1959).
[11]H. G. Dehmelt, "Radiofrequency spectroscopy of stored ions I: Storage," Adv. Atomic Mol. Phys. **3**, 53–72 (1968).
[12]Gina Visan and Ovidiu S. Stoican, "An experimental setup for the study of the particles stored in an electrodynamic linear trap," Rom. J. Phys. **58**, 171–180 (2013).
[13]S. Schlemmer, J. Illemann, S. Wellert *et al*., "Nondestructive high-resolution and absolute mass determination of single charged particles in a three-dimensional quadrupole trap," J. Appl. Phys. **90**, 5410–5418 (2001).
[14]Y. Cai, W.-P. Peng, S.-J. Kuo *et al*., "Single-particle mass spectrometry of polystyrene microspheres and diamond nanocrystals," Anal. Chem. **74**, 232–238 (2002).
[15]Sung Cheol Seo, Seung Kyun Hong, and Doo Wan Boo, "Single nanoparticle ion trap (SNIT): A novel tool for studying in-situ dynamics of single nanoparticles," Bull. Korean Chem. Soc. **24**, 552–554 (2003).
[16]W. P. Peng, Y. C. Yang, M. W. Kang *et al*., "Measuring masses of single bacterial whole cells with a quadrupole ion trap," J. Am. Chem. Soc. **126**, 11766–11767 (2004).
[17]Zhiqiang Zhu, Caiqiao Xiong, Gaoping Xu *et al*., "Characterization of bioparticles using a miniature cylindrical ion trap mass spectrometer operated at rough vacuum," Analyst **136**, 1305–1309 (2011).
[18]H. Winter and H. W. Ortjohann, "Simple demonstration of storing macroscopic particles in a 'Paul trap'," Am. J. Phys. **59**, 807–813 (1991).
[19]Scott Robertson and Richard Younger, "Coulomb crystals of oil droplets," Am. J. Phys. **67**, 310–315 (1999).
[20]L. M. Vasilyak, V. I. Vladimirov, L. V. Deputatova *et al*., "Coulomb stable structures of charged dust particles in a dynamical trap at atmospheric pressure in air," New J. Phys. **15**, 043047 (2013).
[21]K. G. Libbrecht, Newtonian Labs, <http://newtonianlabs.com/> (2018).
[22]S. Earnshaw, "On the nature of the molecular forces which regulate the constitution of the luminiferous ether," Trans. Cambridge Philos. Soc. **7**, 97–112 (1842).
[23]M. V. Berry, "The Levitron: An adiabatic trap for spins," Proc. Roy. Soc. A **452**, 1207–1220 (1996).
[24]C. Sackett, E. Cornell, C. Monroe, and C. Wieman, "A magnetic suspension system for atoms and bar magnets," Am. J. Phys. **61**, 304–309 (1993).
[25]L. D. Landau and E. M. Lifshitz, *Mechanics*, 3rd ed., Course of Theoretical Physics, Vol. 1 (Pergamon Press, Oxford, 1989), p. 93ff.
[26]William B. Whitten, Peter T. A. Reilly, and J. Michael Ramsey, "High-pressure ion trap mass spectroscopy," Rapid Commun. Mass Spectrom. **18**, 1749–1752 (2004).
[27]Michael Nasse and Christopher Foot, "Influence of background pressure on the stability region of a Paul trap," Eur. J. Phys. **22**, 563–573 (2001).
[28]Eugene A. Vinitsky, Eric D. Black, and Kenneth G. Libbrecht, "Particle dynamics in damped nonlinear quadrupole ion traps," Am. J. Phys. **83**, 313–319 (2015).
[29]Jarda Stárek, "Paul Trap," <http://www.youtube.com/watch?v=pqfG-df5ZWk> (2012).
[30]Jarda Stárek, "Paul Trap," <http://www.paultrap.jecool.net/en/> (2012).
[31]B. P. Binks, J. H. Clint, G. Mackenzie, C. Simcock, and C. P. Whitby, "Naturally occurring spore particles at planar fluid interfaces and in emulsions," Langmuir **21**, 8161–8167 (2005) (Image provided by the authors).
[32]Published by username "J B," Paul Traps, <https://www.youtube.com/watch?v=bkYXNeJ8IP0> (2009).

A flexible positron spectrometer for the undergraduate laboratory

Jason Engbrecht[a] and Nathaniel Hillson
Department of Physics, St. Olaf College, Northfield, Minnesota 55057

(Received 28 September 2017; accepted 24 April 2018)

Positron physics touches on a wide-ranging variety of fields from materials science to medical imaging to high energy physics. In this paper, we present the development of a flexible positron annihilation spectrometer appropriate for the undergraduate laboratory. Four NaI gamma-ray (γ-ray) detectors are connected to an oscilloscope-based data acquisition system. Coupled with the software we developed, these detectors allow students to explore a variety of positron and γ-ray phenomena. These include γ-ray energy spectroscopy, Compton scattering, PET scanning fundamentals, speed of light measurements with γ-rays, historically important polarimetry of annihilation radiation, 3-γ annihilation radiation observations, and positron lifetime spectroscopy of materials. We present the developed apparatus and examples of experiments it can perform here. A website, https://wp.stolaf.edu/physics/positron-laboratory-for-undergraduates/, has also been developed to present supplementary materials including apparatus drawings, laboratory write-ups, developed software, and an instructors' manual.
https://doi.org/10.1119/1.5038672

I. INTRODUCTION

With its discovery in 1932 by Carl Anderson, the positron began the era of antimatter in physics. Unlike its antimatter counterparts, the antiproton and antineutron, the positron can be produced from radioactive sources. As such positrons are available for a large array of applications. PET scans,[1] materials science,[2,3] QED tests,[4] fundamental symmetry

experiments,[4] and antihydrogen spectroscopy[5–8] are some of the many areas in which positrons have found applications both historically and in the modern day.

The accessibility of positrons has also brought them to the teaching laboratory. Experiments for undergraduate laboratory classes have been presented in the literature in the past.[9–15] Each of these experiments in literature, while fine examples, focused on one aspect of positron physics with a dedicated apparatus.

With this work we set out to build a single apparatus along with data acquisition software that would allow students to explore the variety of physics accessible with positrons. With that in mind, we focus on detectors and acquisition software that provide maximum flexibility. This paper presents the apparatus and software developed for this purpose. Additionally, it presents examples of experiments performed with this apparatus. The scope of this work makes it necessary to be brief on a variety of aspects of the implementation. Therefore, a website has been developed, https://wp.stolaf.edu/physics/positron-laboratory-for-undergraduates/, with a variety of supplementary information.

The existence of commercially available radioactive sources that produce positrons is key to making experiments such as those presented here accessible to the undergraduate laboratory. The most common choice of source is ^{22}Na with a decay scheme shown in Fig. 1. With a 2.6-year half-life, ^{22}Na is long-lived enough that data rates are stable throughout the course of an undergraduate lab experience. An additional property of value for ^{22}Na is the production of a 1275 keV γ-ray shortly after the emission of the positron. This γ-ray comes from the excited state of ^{22}Ne that is formed during the emission of the positron. The short lifetime of this excited state (3.7 ps) is essentially instantaneous for the purpose of all the experiments presented here. Thus, the detection of this 1275 keV γ-ray can serve as a positron creation signal in timing experiments.

The positron, once emitted, will do one of two things. It can either find an electron and directly annihilate with it or it can find an electron and bind with it, forming the electron-positron bound system called positronium (Ps). Ps can form in either the $S = 0$ state (para-Ps) or the $S = 1$ state (ortho-Ps). Direct annihilation and para-Ps annihilation both decay into 2 γ-rays. Time scales for these 2–γ annihilations are typically a few hundred picoseconds.

Ortho-Ps has a much longer lifetime of 142 ns in a vacuum because its spin does not allow it to decay into 2 γ-rays and instead it produces 3 γ-rays during annihilation. However, in the dense medium of a solid, the positron in the electron-positron pair will usually find an alternate electron that is more favorably aligned to allow it to decay via a 2–γ annihilation. Thus, in most solid materials any ortho-Ps formed will have its lifetime reduced, typically to a few nanoseconds.

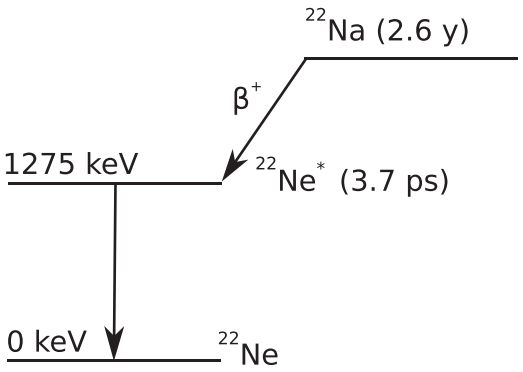

Fig. 1. Decay Scheme of ^{22}Na.

The net result of all these positron interactions is that the overwhelming majority of positrons will annihilate with an electron within a few nanoseconds and form 2 γ-rays. Conservation of energy and momentum demand that these 2 γ-rays will be of equal energy (511 keV) and will travel in anti-parallel directions. This annihilation pair has some distinct experimental advantages when compared to other γ radiation from radioactive sources. Detecting both γ-rays in the pair can be used to locate the source of the radiation, to reduce random background radiation, and to allow for polarimetry. All of these advantages are demonstrated in experiments presented in this paper.

A. Safety

The ^{22}Na sources used in the experiments described here are all 10 μCi or below. This level of activity is the largest allowed for a ^{22}Na source to be exempt from licensing requirements. However, while the required sources are all exempt, their use still necessitates proper radiation safety awareness. Sources that are going unused should be stored behind proper lead shielding at all times. While it is safe to handle the sources in the course of running the laboratory, students should be encouraged to minimize their exposure time. Finally, in the experiments that utilize the lead collimator, we describe stacking two 10 μCi sources together. Stacking the two sources creates a source that is no longer exempt and thus licensing would be necessary. An alternative approach would be to use only one 10 μCi source. The moderate increases in data acquisition times caused would be quite manageable.

II. APPARATUS

In order to facilitate wider adoption of the presented work, when designing the apparatus attention was paid to cost and use of commercially available parts. It is estimated that the entire experiment can be reproduced for approximately $11,000. A moderate amount of 3D printing and machining was used to create the experimental setup using skills and tools available in most department machine shops. The custom-built power supply used in this work can be straightforwardly reproduced or replaced with commercial bench top supplies for a reasonable cost increase. Detailed drawings and parts lists for all of the custom built parts can be found at the previously mentioned website. Table I shows the equipment list for the present work as well as estimated costs.

Table I. Equipment list and costs.

Item	Cost
NaI detectors	$5,500
USB oscilloscope and cables	$3,500
^{22}Na sources	$500
Lead collimator	$200
HV power supply	$1,000
Miscellaneous hardware and 3D printing	$200
Total	$10,900

Fig. 2. NaI detector with integrated photomultiplier shown with two 3D printed holders.

The foundation of the experimental apparatus is four 51 mm × 51 mm cylindrical NaI scintillation crystals paired with photomultipliers. The detector/photomultiplier package is a commercial package from Scionix Holland, 51B51/2M-E1-X2-NEG. The photomultiplier anode output is connected directly to the oscilloscope with 50 Ω input impedance and without a preamplification stage. We used NaI-based detectors to give the best balance of energy resolution, timing resolution, detection efficiency and affordability for γ-ray detection. Modern crystals such as BaF_2 or $CeBr_3$ have superior timing properties to NaI. However, pricing of these crystals was between 3 and 10 times higher than NaI so we decided to pursue the more economical model. The NaI detectors can be reconfigured into a variety of orientations for different experiments. To facilitate this, a number of 3D printed mounts were produced to secure and protect the detectors. A detector and two of these holders are shown in Fig. 2. A custom-made 4-channel negative 2 kV variable power supply was built to power the detectors. After pulse processing, these detectors exhibited an energy resolution of 8.4% FWHM (at 511 keV) and a timing resolution of 2.4 ns.

The electrical pulses from the NaI detectors are traditionally processed by dedicated pulse-processing electronics. As an example, timing between two detectors is often done using two Constant-Fraction Single Channel Analyzers that locate the pulses in time. These are fed to a Time-to-Analog Converter to produce a new pulse proportional in height to the time between the signals. Finally, this is sent to a Multi-Channel Analyzer that digitizes the pulse for a computer. This electronics system alone can easily cost about $10,000. While an energy spectroscopy system is somewhat more straightforward, a Multi Channel Analyzer system for a single channel can still range in cost from $1500 to $5000. In order to achieve the flexibility desired for this apparatus using 4 channels simultaneously, an alternative needed to be pursued.

To reduce costs and substitute for the traditional pulse processing electronics, we chose to use a USB-based oscilloscope. The oscilloscope chosen was the 4-channel PicoScope 6402D, a 250 MHz bandwidth oscilloscope with a sample rate of 5 GS/s. The sample rate is shared between active channels so that with all channels active the effective sample rate is 1.25 GS/s. This oscilloscope allows the computer to capture the raw pulse data for each detection event and process it in software for energy and timing information. The oscilloscope has sufficient capabilities such that, when paired with NaI detectors, software can analyze pulses with the same energy and timing precision of dedicated electronics. The major sacrifice is data throughput. Our system currently achieves throughputs of approximately 1000 events/s compared to dedicated systems that can achieve 10–100 times faster throughput. This throughput is limited by the capabilities of the oscilloscope USB communication with LabView which is controlled by manufacturer supplied drivers. No exceptional measures were needed for the software, described later in this paper, to keep up with analysis of this data throughput. However, our achieved throughput is sufficient for all the experiments proposed here.

We utilize two types of commercially available ^{22}Na radioactive sources to produce positrons. For most experiments, only the γ-rays from annihilation are needed. For these, a 10 μCi plastic source in which the positron primarily annihilates in the source encapsulating material is used. For experiments in which the positrons need to exit the source, Positron Lifetime Spectroscopy and 3-γ Annihilation Radiation, a 10 μCi source in which the ^{22}Na is sealed under a thin sheet of Mylar is used. With a 2.6 year half-life, these sources will need to be replaced about every 3 years.

For a number of experiments, the γ-ray annihilation radiation needs to be collimated. For these experiments, we have a lead house for γ-ray collimation in which two standard (non-mylar covered) 10 μCi sources are placed in the center, as shown in Fig. 3. Non-standard lead bricks were machined in-house.

III. SOFTWARE

The software for these experiments was developed using the LabView development platform. In developing the

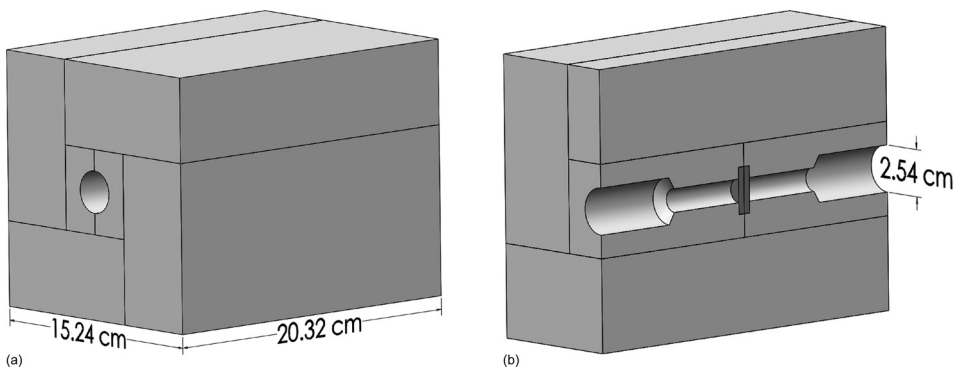

Fig. 3. Lead house used to produce collimated back-to-back γ-rays from 2-γ annihilation radiation.

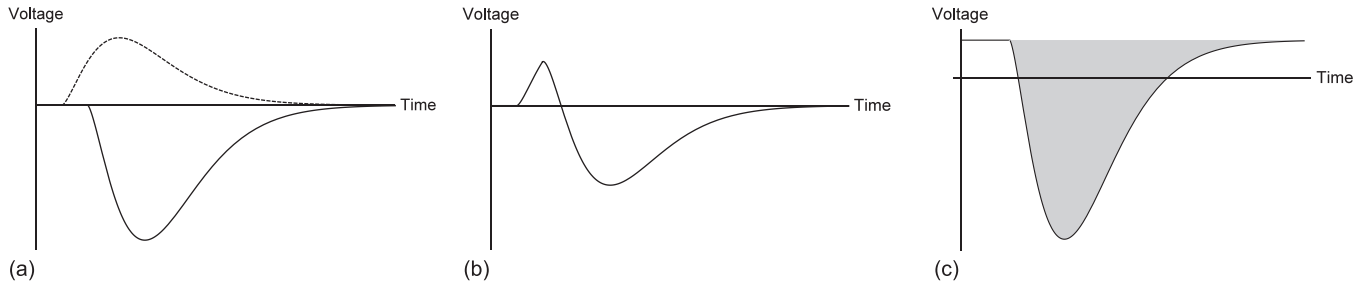

Fig. 4. (a) The process of Constant Fraction Discrimination in which a pulse is multiplied by a fraction and time shifted. (b) The result of adding the two signals in (a) creating a zero crossing that can be used for timing. (c) The shaded area represents the integration of a pulse while correcting for small zero offsets. The result is proportional to the energy deposited by the detected γ-ray.

software we wanted to avoid experiment-specific interfaces that might inhibit the students' opportunity to explore. Instead, we developed a set of general spectroscopic tools that could be applied to a variety of experiments. All software described here can be found on the website described earlier in this paper.

As data are acquired from the oscilloscope, the software performs analysis of the pulses from each detector. Figure 4 shows how this process works. Pulse area is proportional to the energy of the detected γ-ray and thus a simple numerical integration with background correction is used to determine the γ-ray energy. In order to determine the timing of each pulse a constant fraction method is used. In this method, the pulse is inverted, scaled and time shifted before being added to the original pulse. The result is then examined for a zero crossing to locate the pulse in time. The pulses produced by our detectors have a pulse shape that depends somewhat on pulse height. To combat that, the delay used to timeshift the inverted pulse is short, consistent with Amplitude and Rise Time Compensation techniques. Once each pulse is analyzed for its timing and energy information, the original oscilloscope trace is erased from memory. The energy and timing information are cataloged for every pulse to be used in later analysis.

The user interface consists of six selectable panels that provide interfaces to users for examining the pulse energy and timing information stored in memory. Figure 5 shows the program with the Energy Plots panel chosen.

The panels labeled Data Acquisition and Calibrate are used to prepare the acquisition system for acquiring data. The Data Acquisition panel allows the user to choose how data is acquired. Data can be acquired until user intervention or until presets for acquisition time or event numbers. From the panel the user can determine which detectors are being used and any coincidences that are required. In this panel, all available event data (timing and energy) can be downloaded for offline analysis. The Calibration panel allows the user to calibrate the area/energy conversion needed for turning the pulse areas into energy measurements. This is an automated process completed by simply putting a ^{22}Na source near all of the detectors and using the software to activate the calibration procedure.

The Energy Plots, Timing Plots, and Energy Sum Plots panels are all similar in their function. They allow users to look at a variety of histograms of the data. The Energy Plots and Energy Sum Plots both provide energy histograms but the Energy Sum Plots panel sums the energy of selected detectors before creating the histogram of the results. The Timing Plots panel creates a histogram of the time between events in two different detectors. This timing histogram can also be filtered by energy to allow only certain types of events

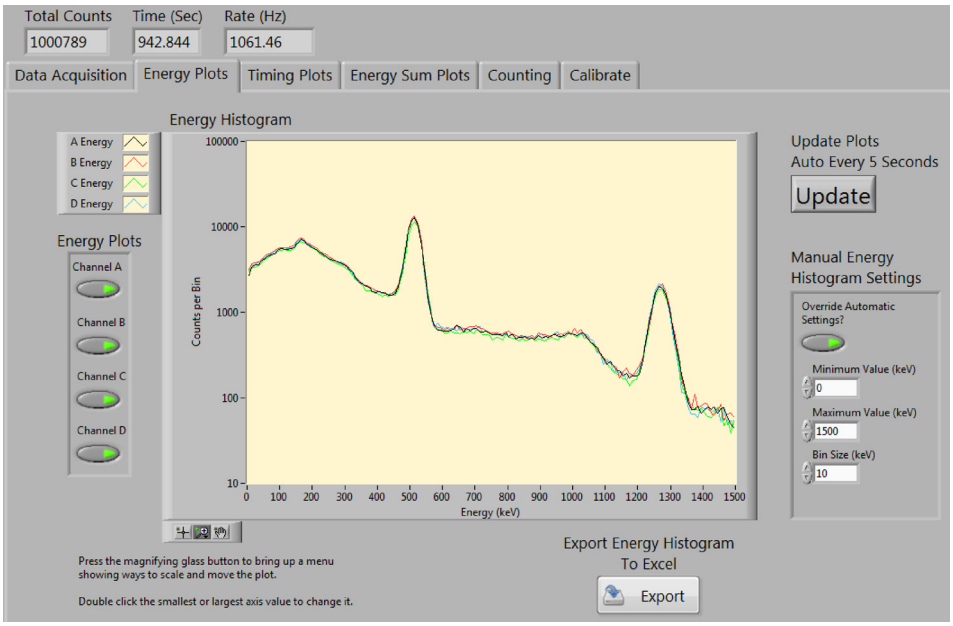

Fig. 5. The user interface for the data acquisition software showing the Energy Plots panel.

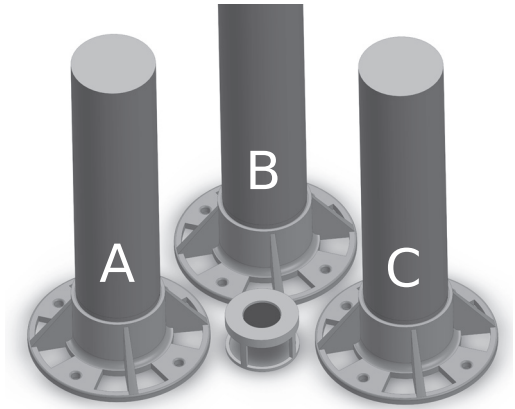

Fig. 6. Detector and source setup for γ-ray spectroscopy experiment.

to be included. The users have control over the limits of the histograms and the binning of the histograms if desired. The histograms' data can also be downloaded for offline use.

The Counting panel allows the user to count events that meet specified timing and energy restrictions. Multiple settings can be examined simultaneously.

All of the software described here can be found at the previously mentioned Website (https://wp.stolaf.edu/physics/positron-laboratory-for-undergraduates/) in the formats of both the original Labview code and as a stand-alone executable.

IV. EXPERIMENTS

The apparatus developed is currently planned to be placed into two laboratory courses at St. Olaf College. The first lab is our Modern Physics Laboratory for sophomore-level physics majors. In this lab, students have two 3-hour sessions to complete the experiments. The second lab is our Advanced Laboratory for junior-level physics majors. In this lab, students have three 3-hour sessions for their week. Each lab course has a unique set of experiments. In the junior level laboratory there is also an option for students to pursue some of the experiments presented here in more depth for an additional three weeks. Most of the experiments described here can acquire data within the time period allotted for a laboratory session. The exceptions are the Polarimetry of Annihilation Radiation experiment and the 3–γ Annihilation Radiation experiments which both require at least 3 h of data acquisition time.

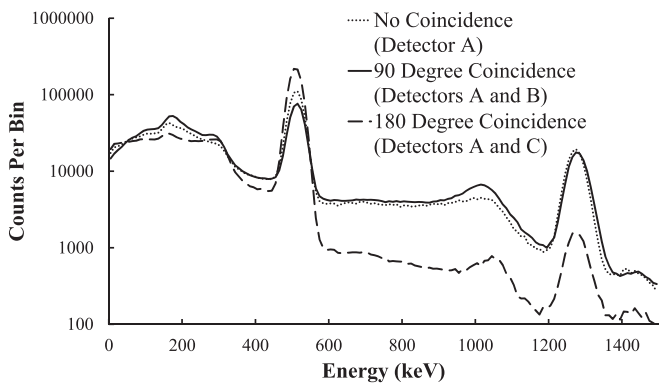

Fig. 7. γ-ray spectroscopy result using the detector setup of Fig. 6. Changing coincidence configurations alters the system's response to 511 keV vs 1275 keV γ-rays.

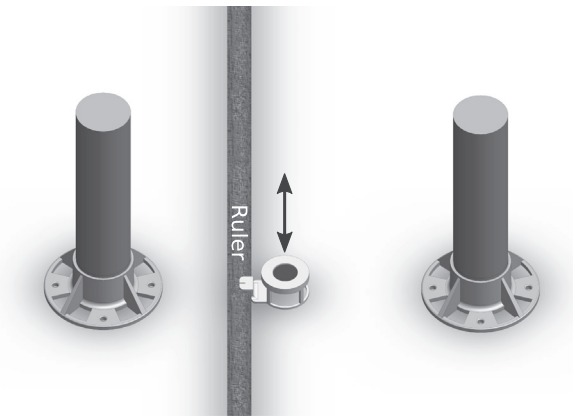

Fig. 8. Experimental setup for the PET scanning demonstration. A source located between two detectors is moved along the shown ruler while event rates are measured.

We present all the experiments developed here, organized as they are presented in our laboratory courses. Write-ups for students as used in our laboratory are available on the previously mentioned website. These experiments are ordered to allow students to developed needed skills with simpler experiments early on that allow to complete the more complex experiments at a later date. Adopters of this apparatus could mix and match the developed experiments in a variety of ways as is suitable for their laboratory structure.

V. MODERN LAB EXPERIMENTS

The goal of the Modern Lab experiments is to introduce students to the basics of the apparatus and software, as well as the fundamental properties of positron annihilation. They are by design shorter experiments that can be completed in a straightforward manner.

A. γ-ray spectroscopy of annihilation radiation

This experiment introduces the students to the idea of γ-ray energy spectroscopy, in particular, for annihilation radiation. A ^{22}Na source is placed in a holder on the table as a source of 1275 keV and 511 keV-pair γ-rays. Two NaI detectors are placed in holders that allow for the students to vary the geometry of the system. In the software students can examine the effect of demanding coincidences between the two detectors.

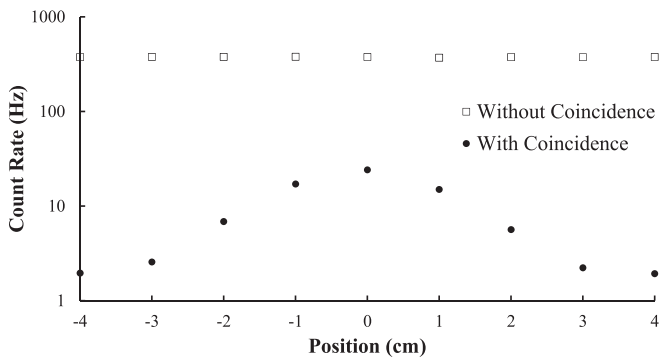

Fig. 9. PET scanning data showing variation of data rates with source position. The use of coincidence detection clearly enhances the ability to infer the position of radiation as shown by the enhanced peak in data rates. Error bars are smaller than the points plotted and thus are omitted.

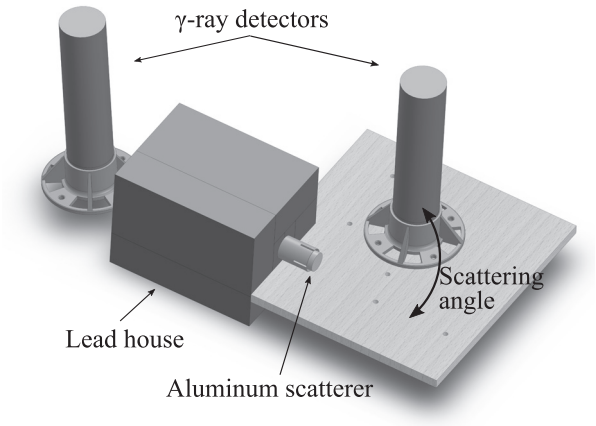

Fig. 10. Compton scattering setup to measure scattered γ-ray energy at a scattering angle of 60°.

Figure 6 shows three detectors surrounding a ^{22}Na source. Energy spectra are acquired with a variety of detector coincidence configurations with the example results shown in Fig. 7. Using only one detector (detector A) compared to demanding a coincidence between detectors A and B shows a slight suppression of 511 keV γ-ray detections. In contrast, with detectors A and C in coincidence, the 511 keV detections are greatly enhanced while the 1275 keV detections are suppressed. These changes in the spectrum are due to the correlation in direction between the 511 keV γ-rays and the lack of such a correlation with the 1275 keV γ-rays. Students are asked to consider and comment on these changes.

B. PET scanning fundamentals

To further explore the nature of the 511 keV γ-rays emitted from positron annihilation, students are asked to explore how the nature of these γ-rays is used in PET scans. Two detectors are placed 50 cm apart with a ^{22}Na source between them, as shown in Fig. 8. The source is then moved off-axis from between the detectors and the rate is tracked for each detector individually as well as for the coincidence between them. Figure 9 shows an example of the type of data acquired and the enhancement for locating the source of the radiation using the coincidence.

C. Low-noise Compton scattering

This experiment utilizes the lead house for producing collimated 511 keV γ-ray pairs as shown in Fig. 10. A 25 mm × 25 mm Aluminum cylinder is placed at one output port of the lead house to Compton scatter γ-rays. One NaI detector is placed at the other port in order to detect the non-scattered γ-ray from the pair. The second NaI detector is then placed to detect a scattered γ-ray at scattering angles of 0°–90° in 15° increments.

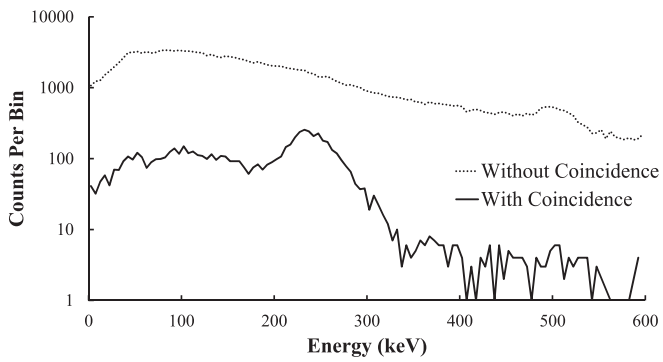

Fig. 11. γ-ray energy spectrum for Compton scattering at 90° with and without demanding a coincidence with the 511 keV pair γ-ray. At this angle, the scattered photon energy is predicted to be 255 keV. The peak at this energy is clearly enhanced using the coincidence technique.

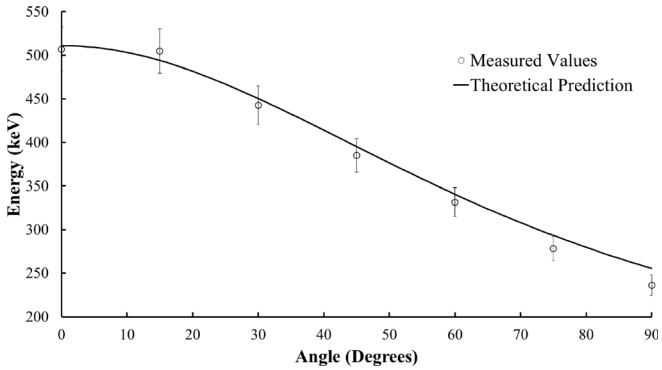

Fig. 12. Measured values for Compton scattered γ-rays compared to theoretical predictions.

The scattering rate from the Aluminum cylinder is much too low to be detected above background signals. Thus, in order to observe the Compton scattered γ-rays the background must be reduced. Fortunately the two back-to-back γ-rays produced provide an opportunity to do this by demanding a coincidence between both γ-rays. Figure 11 shows the advantage of demanding a coincidence between both detectors in reducing the background noise in the signal. This reduction in noise allows the students to make accurate measurements of energy for the scattered γ-rays that they can use to confirm Compton's relativistic prediction

$$\frac{1}{E'} - \frac{1}{E} = \frac{1}{E_0}(1 - \cos(\theta)). \tag{1}$$

Here, E is the incident photon energy, E' is the photon energy after scattering, E_0 is the electron rest energy, and θ is the scattering angle. Example measurements are shown in Fig. 12.

D. γ-ray velocity measurement

In this experiment, students make a direct measurement of the velocity of γ-rays. This measurement helps to identify γ-rays as electromagnetic radiation by confirming that they indeed travel at the speed of light. Figure 13 shows the experimental setup. A ^{22}Na source is set in between two

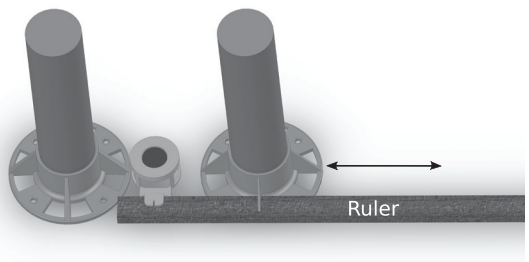

Fig. 13. Experimental setup for measurement of γ-ray velocity. The detector on the right is moved along the ruler to create time delays that can be measured.

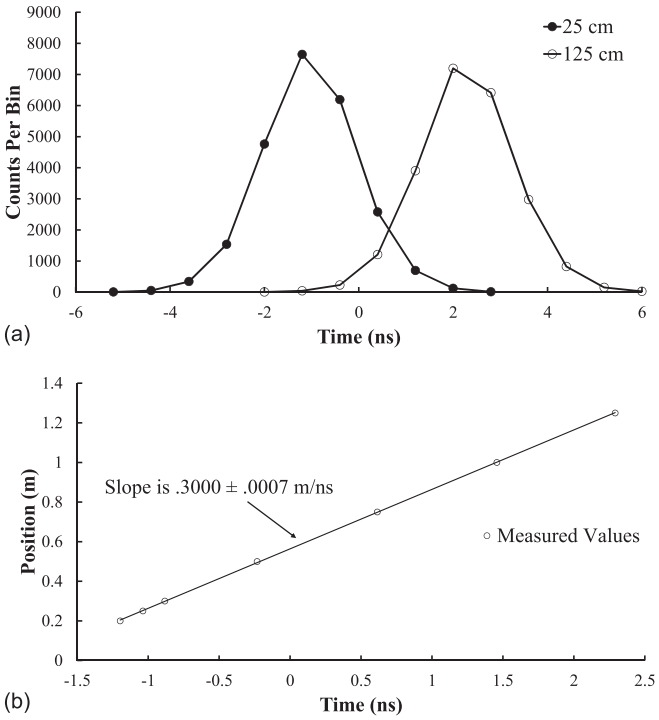

Fig. 14. (a) Timing histograms between two detectors shown for two different separation distances. These peaks can be fitted to determine their center for timing purposes. (b) Plot of the time delays with increasing distance. The slope represents the γ-ray velocity and is consistent with the speed of light as expected. Error bars in both (a) and (b) are smaller than the points plotted and thus are omitted.

detectors and the timing between signal arrivals is measured. One of the detectors is then moved incrementally away from the source and the timing between signals is measured at each position. Figure 14 shows an example of the data acquired and the evident time delays.

VI. ADVANCED LABORATORY

The advanced laboratory experiments are designed to allow students to delve further into experimental techniques using positron annihilation. The individual experiments are more involved and offer the students the opportunity to explore on their own.

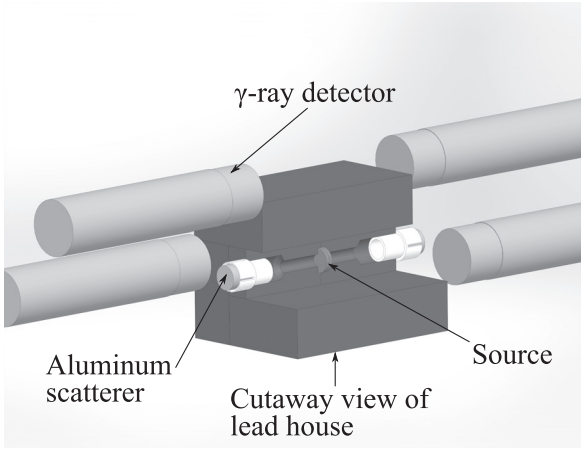

Fig. 15. Experimental setup for performing γ-ray polarimetry with cross-section of lead house removed. Aluminum scatterers are placed at both exits of the lead house. NaI detectors are placed on both sides of the lead house to allow simultaneous detection of Compton scattering for both γ-rays in an annihilation 511 keV pair.

A. Polarimetry of annihilation radiation

1. Experiment

The back-to-back 511 keV γ-ray radiation from the positron-electron annihilation radiation provides an excellent opportunity to study an entangled pair system. As discussed earlier in this paper, in solid materials the positron-electron pairs usually annihilate from the $S=0$ state, creating a pair of 511 keV γ-rays. The spin state of the annihilating pair also determines the polarization of the entangled pair of γ-rays. The linear polarization state of the γ-rays can be described[16,17] as

$$\frac{1}{\sqrt{2}}\left(|\updownarrow\rangle_1|\leftrightarrow\rangle_2 - |\leftrightarrow\rangle_1|\updownarrow\rangle_2\right). \tag{2}$$

Here, the $\updownarrow$ and $\leftrightarrow$ are polarizations and 1 and 2 are the back-to-back directions of travel.

To experimentally examine this polarization correlation, we can use the fact that Compton scattering is in fact angularly correlated to the polarization of the scattering γ-ray, a relationship first derived using QED by Klein and Nishina,[18]

$$\frac{d\sigma}{d\Omega} = \frac{r_e^2}{2}\left(\frac{E'}{E}\right)^2\left[\frac{E'}{E}+\frac{E}{E'}-2\sin^2(\theta)\cos^2(\phi)\right]. \tag{3}$$

Here, r_e is the classical electron radius (equal to $e^2/(4\pi\epsilon_0 m_e c^2)$), E is the energy of the incident photon, E' is the energy of the scattered photon, θ is the scattering angle, and ϕ is the angle between the incident photon's polarization and the scattering direction.

To use this effect to perform polarimetry on the annihilation radiation, two aluminum cylinders are placed on either side of the lead house to Compton scatter γ-rays. The 4 NaI detectors are placed around the lead house as shown in Fig. 15 in order to detect γ-rays that scatter at 90°. The acquisition system is then set up to look for coincidences between pairs of detectors. Because the pairs of γ-rays are in a state in which they are cross-polarized, coincidences should be favored in detectors that are separated axially by 90° ($\Delta\phi = 90°$) over those separated by 0° ($\Delta\phi = 0°$) and 180° ($\Delta\phi = 180°$). The relative probability for pairs of scattered γ-rays to be detected is expressed by

$$\rho = \frac{R_{90°}}{R_{0°}} = 1 + \frac{2\sin^4(\theta)}{\gamma^2 - 2\gamma\sin^2(\theta)}, \tag{4}$$

where

$$\gamma = 2 - \cos(\theta) + \frac{1}{2-\cos(\theta)}. \tag{5}$$

Here, $R_{90°}$ and $R_{0°}$ are the event rates at $\Delta\phi = 90°$ and 0°, respectively. It should be noted that $R_{0°} = R_{180°}$. This follows from Eqs. (2) and (3), a full derivation of which can be seen elsewhere.[16,17]

Assuming infinitesimally small solid angles for the detectors, Eq. (4) predicts $\rho = 2.6$ when $\theta = 90°$. Experimentally we found $\rho = 2.4 \pm 0.1$. This was looking at coincidence rates for events in the energy range 245–265 keV, a range

that is centered on the predicted energy of Compton scattered annihilation gamma rays of 255 keV. Given that the solid angles of acceptance are substantial this is a surprisingly good result. This indicates that although the acceptance angles are not ideal, the desired scattering angles are highly favored.

Currently, this experiment is limited to study of a single angle due to apparatus limitations. The long data acquisitions times (at least 3 h) would likely necessitate the use of a motorized and automated system to study multiple angles in the context of a student laboratory. While we are considering this for future development, it is not currently part of the apparatus.

2. *Historical context*

In addition to examining the polarization of the γ-rays from positron annihilations, this experiment replicates some of the earliest experiments used to look at entanglement and the EPR paradox.[19] This annihilation pair was first theoretically examined independently in two papers.[16,17] Experimentally, this system was then studied by Wu and Shaknov[20] in 1950. Later, as other theoretical works were attempting to understand the paradox of EPR,[21] Bohm and Ahronov[22,23] argued in 1957 that this earlier positron polarimetry work in fact was evidence that the properties of quantum mechanics criticized by the EPR paradox were in fact real properties of matter.

After the work of Bell[24] in 1964, it was understood that similar correlation experiments could be used to rule out all hidden variable theories. In light of this work, Kasday *et al.*[25] performed an update to the experiment of Wu and Shaknov[20] in 1974 in order to interpret the results of the technique as a Bell's Inequality experiment. In that work and later work[26] it has been shown that hidden variable theories can in fact replicate the result of the Klein-Nishina equation. Thus, the result of any correlated polarization experiment that uses Compton scattering as the mechanism for the polarimetry can also be reproduced by local hidden variable theories. Therefore, while these types of experiments are important for historical context, they have been replaced by other techniques in modern experiments.

B. Positron lifetime spectroscopy

When introduced into a solid material, a positron will follow one of a few paths to annihilation. On the short time scale they can form para-Ps or find an electron to directly annihilate with. Direct annihilation typically takes a few hundred picoseconds while para-Ps decays exponentially with a lifetime of 125 ps. Both of these time scales are significantly less than the 2.4 ns timing resolution of our detectors and thus will simply show up as a timing peak in our system.

The other path for annihilation occurs when the positron binds with an electron and forms ortho-Ps. This three-γ annihilation has a much longer lifetime of 142 ns in vacuum. In a solid material, this will be reduced greatly by the interaction of the Ps with the material. The positron in the bound system can find an electron other than its bound partner to annihilate with, reducing its lifetime in a process called "pick-off."

Thus, the lifetime of o-Ps in a material can be used to study the void properties of the materials it is in. When voids of $\sim$1 nm in size are available, the lifetime can be used to quantitatively measure the size of the voids using the Tao-Eldrup model[27]

$$\tau = \frac{0.5\,\text{nanoseconds}}{1 - \dfrac{R}{R + 0.166\,\text{nm}} + \dfrac{1}{2\pi}\sin\left(\dfrac{2\pi R}{R + 0.166\,\text{nm}}\right)}. \quad (6)$$

This semi-empirical equation gives the lifetime of ortho-Ps (τ) as a function of the radius of the voids in the material (R).

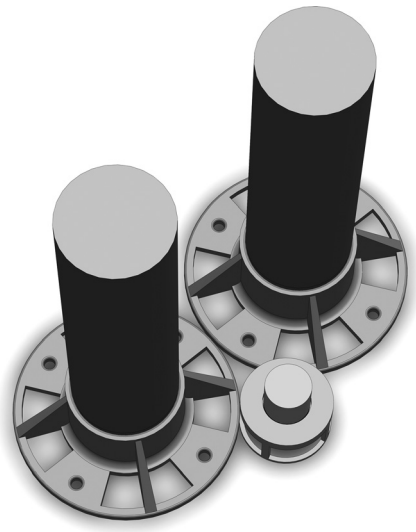

Fig. 16. Positron lifetime spectroscopy experiment setup.

The setup for the experiment is simple. A ^{22}Na source (the 2 μCurie source with a thin Mylar window) is placed at 90° to two detectors as shown in Fig. 16. While not critical, the 90° angle reduces the number of counts triggered by back-to-back annihilation γ-rays. A sample material of interest is placed on top of the source and the timing is measured between 1275 keV γ-rays and annihilation γ-rays. Figure 17 shows the timing spectra of two samples. The Aluminum, as a metal, does not form Ps (Ref. 4) and thus has a shorter lifetime than the Silicone sample.

At the current time, this experiment as developed is only qualitative, but future development may expand this component to be quantitative. The Silicone, with a Ps lifetime of

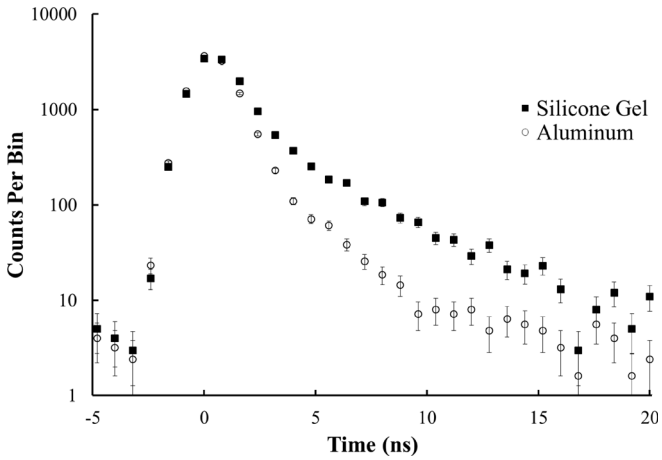

Fig. 17. Positron lifetime spectroscopy data. Silicone and Aluminum show clear differences in positron/positronium lifetime due to the difference in positron interactions in the two materials.

about 4 ns, could be studied quantitatively by students if desired. To do this serious consideration would need to be given to background signals and detector resolution. Positrons do enter the plastic that encapsulates the ^{22}Na source as well as the desired samples. Thus there is a competing signal in the timing spectrum and quantitative analysis requires more exploration than typical lab times allow. However, with additional time, student can explore techniques for identifying the competing signals as well as how to convolve the detector resolution with the exponential decay signal.

C. 3-γ annihilation radiation

The o-Ps 3-γ decay channel is difficult to observe without concerted effort. In a solid material, the dominant effect is pick-off and 2-γ decay. In order to achieve a significant amount of 3-γ annihilation, the Ps needs to form in a diffuse environment such as a gas.

We achieve this environment by placing fumed silica powder on a ^{22}Na source. The powder helps keep the positrons from the ^{22}Na source contained to a small space, but also allows for any Ps formed to exist in large open volumes. In our system, the air that fills the space within the powder is still able to reduce the o-Ps lifetime from 142 ns to ~70 ns via pick-off. Nevertheless, a large fraction of the o-Ps can decay via 3 γ-rays.

The experiment aims to confirm the existence of the 3-γ decay channel. To accomplish this we use four detectors as shown in Fig. 18. Three of these detectors are co-planar while the fourth detector is placed above the others. Coincidence is demanded between all four detectors. Events that are detected are filtered in two ways.

(1) The three co-planar detector events are examined for timing to ensure that the detections occurred with a 10 ns window.
(2) The fourth detector is required to have an energy of 1275 keV.

The resulting data can be plotted as shown in Fig. 19. This figure shows the energy of a single detector vs. the sum of the energies of the three co-planar detectors. A clear signal of 3-γ events is the highlighted area in the figure. The highlighted area is at 1022 keV in the sum of the detectors indicating that all three detectors add up to the appropriate energy of the positron-electron annihilation. The area does not extend up to 511 keV for a single detector. This is important as it indicates that the signals are not 2-γ pairs in which one γ-ray

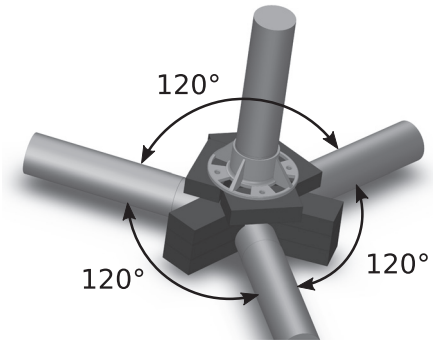

Fig. 18. Experimental setup for 3-γ detection. Three detectors are placed so as to be coplanar and separated by 120°. Lead is placed between the detectors to reduce scattering between them. The top detector is used to detect the coincident 1275 keV γ to further reduce accidental coincidences.

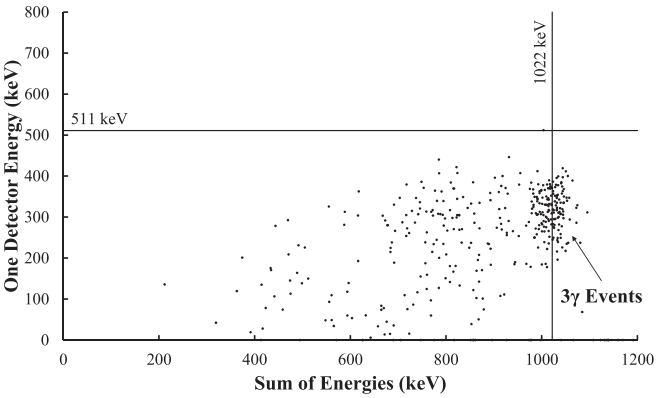

Fig. 19. Scatter plot of detected events for the 3-γ detection experiment. Lines at 511 keV for the single detector energy and 1022 keV for the 3 detector energy sum are shown for reference. A clear accumulation of events can be seen in the expected region for 3-γ events as indicated.

scattered from one detector into the other. The events below 1022 keV in the sum represent times in which one (or more) of the gamma rays scattered from the detector and thus did not leave all of its energy in the scintillation crystal.

VII. CONCLUSION

The experiments presented here represent a diverse and flexible set of learning experiments for students. In addition to the examples presented here, there are opportunities for students to explore further. Examples include:

(1) Looking at a wide variety of samples to develop models of the Ps lifetime in materials.
(2) Replacing the air in the fumed silica with other gasses to get better measurements of the o-Ps lifetime.
(3) Increasing the precision of the speed of light measurement with more data acquisition and precise position measurements.

In the future, we hope to develop the apparatus further to allow for more flexibility. Ideas include:

(1) Placing a source in a container in which gas content and pressure can be controlled to allow for careful measurement of the o-Ps lifetime as a test of QED.[12]
(2) Passing the detector signals through an FPGA in order to get accurate rate measurements when rates are higher than accessible by the oscilloscope.
(3) Expanding the software to include more data presentation tools.
(4) Developing an apparatus for the Polarimetry of Annihilation Radiation experiment that allows multiple scattering angles to be examined.

Finally, in order to promote the adoption of these experiments at other institutions we have made available all the work presented here on the St. Olaf Physics Department website. This includes detailed drawings of the apparatus, software, and lab manuals. These materials will be updated with future progress.

ACKNOWLEDGMENTS

The authors would like to thank St. Olaf College for their financial support in this work as well as our colleagues in the

St. Olaf Physics department who have provided valuable feedback in the development of these experiments.

[a]Electronic mail: engbrech@stolaf.edu

[1]A. M. Granov, *Positron Emission Tomography* (Springer-Verlag, Berlin, 2013).
[2]R. Krause-Rehberg and H. S. Leipner, *Positron Annihilation in Semiconductors: Defect Studies* (Springer-Verlag, Berlin, 1999).
[3]Sergey V. Stepanov and Vsevolod M. Byakov, "Physical and radiation chemistry of the positron and positronium," in *Principles and Applications of Positron and Positronium Chemistry*, edited by Y. C. Jean, P. E. Mallon, and D. M. Schrader (World Scientific, Singapore, 2003).
[4]Michael Charlton and John W. Humberston, *Positron Physics* (Cambridge U.P., Cambridge, 2001).
[5]M. Amoretti *et al*., "Production and detection of cold antihydrogen atoms," Nature **419**(6906), 456–459 (2002).
[6]G. Gabrielse *et al*., "Background-free observation of cold antihydrogen with field-ionization analysis of its states," Phys. Rev. Lett. **89**(21), 213401 (2002).
[7]M. Ahmadi *et al*., "Observation of the hyperfine spectrum of antihydrogen," Nature **548**(7665), 66–69 (2017).
[8]M. Ahmadi *et al*., "Observation of the 1S-2S transition in trapped antihydrogen," Nature **541**(7638), 506–510 (2017).
[9]M. E. A. Elbasher *et al*., "Observation of triple-photon decay in positron-electron pair annihilation: a triple coincidence setup for the undergraduate laboratory," preprint arXiv:1109.3951 (2011).
[10]Jerzy Dryzek and Douglas Singleton, "Test of the second postulate of special relativity using positron annihilation," Am. J. Phys. **75**(8), 713–717 (2007).
[11]Jerzy Dryzek *et al*., "An undergraduate experiment to test relativistic kinematics using in flight positron annihilation," Am. J. Phys. **74**(1), 49–53 (2006).
[12]M. Yuly, "Positronium in the undergraduate laboratory," Am. J. Phys **67**(10), 880–884 (1999).
[13]Luis Peralta, "A simple electron-positron pair production experiment," Am. J. Phys. **74**(5), 457–461 (2006).
[14]John D. McGervey, "Student measurement of fermi energy by positron annihilation," Am. J. Phys. **31**(9), 713–718 (1963).
[15]Sherwood Parker, "Relativity in an undergraduate laboratory—Measuring the relativistic mass increase," Am. J. Phys. **40**(2), 241–244 (1972).
[16]M. H. L. Pryce and J. C. Ward, "Angular correlation effects with annihilation radiation," Nature **160**(4065), 435 (1947).
[17]Hartland S. Snyder, Simon Pasternack, and J. Hornbostel, "Angular correlation of scattered annihilation radiation," Phys. Rev. **73**(5), 440–448 (1948).
[18]Oskar Klein and Yoshio Nishina, "Über die streuung von strahlung durch freie elektronen nach der neuen relativistischen quantendynamik von Dirac," Z. Phys. **52**(11–12), 853–868 (1929).
[19]F. J. Duarte, "The origin of quantum entanglement experiments based on polarization measurements," Eur. Phys. J. H **37**(2), 311–318 (2012).
[20]Chien-Shiung Wu and Irving Shaknov, "The angular correlation of scattered annihilation radiation," Phys. Rev. **77**(1), 136 (1950).
[21]Albert Einstein, Boris Podolsky, and Nathan Rosen, "Can quantum-mechanical description of physical reality be considered complete?," Phys. Rev. **47**(10), 777–780 (1935).
[22]David Bohm and Yakir Aharonov, "Discussion of experimental proof for the paradox of Einstein, Rosen, and Podolsky," Phys. Rev. **108**(4), 1070–1076 (1957).
[23]David Bohm and Yakir Aharonov, "Further discussion of possible experimental tests for the paradox of Einstein, Podolsky and Rosen," Nuovo Cimento (1955–1965) **17**(6), 964–976 (1960).
[24]John S. Bell, "On the Einstein Podolsky Rosen paradox," Physics **1**(3), 195–200 (1964).
[25]L. R. Kasday, J. D. Ullman, and C. S. Wu, "Angular correlation of Compton-scattered annihilation photons and hidden variables," Nuovo Cimento B(1971–1996) **25**(2), 633–661 (1975).
[26]Herbert Dreiner, "Bell's inequality and τ-physics at LEP," preprint arXiv:hep-ph/9211203 (1992).
[27]D. W. Gidley *et al*., "Positronium annihilation in mesoporous thin films," Phys. Rev. B **60**(8), R5157–R5160 (1999).